OPEN ACCESS



JWST Observations of SN 2023ixf. II. The Panchromatic Evolution between 250 and 720 Days after the Explosion

```
K. Medler , C. Ashall , P. Hoeflich , E. Baron , J. M. Der Kacy , M. Shahbandeh , T. Mera , T. M
 C. M. Pfeffer <sup>1,48</sup>, W. B. Hoogendam <sup>1,48</sup>, D. O. Jones <sup>6</sup>, S. Shiber <sup>2</sup>, E. Fereidouni <sup>2</sup>, O. D. Fox <sup>5</sup>, J. Jencson <sup>7</sup>, L. Galbany <sup>8,9</sup>, J. T. Hinkle <sup>1,49</sup>, M. A. Tucker <sup>10,11</sup>, B. J. Shappee <sup>1</sup>, M. E. Huber <sup>1</sup>, K. Auchettl <sup>12,13</sup>, C. R. Angus <sup>14,15</sup>, D. D. Desai <sup>1</sup>, A. Do <sup>16</sup>, A. V. Payne <sup>5</sup>, J. Shi <sup>12</sup>, M. Y. Kong <sup>1</sup>, S. Romagnoli <sup>12</sup>, A. Syncatto <sup>17</sup>, A. Syncatto <sup>17</sup>, A. Syncatto <sup>17</sup>, A. Syncatto <sup>18</sup>, A. Syncatto
C. R. Angus<sup>14,13</sup>, D. D. Desai<sup>1</sup>, A. Do<sup>10</sup>, A. V. Payne<sup>3</sup>, J. Shi<sup>12</sup>, M. Y. Kong<sup>1</sup>, S. Romagnoli<sup>12</sup>, A. Syncatto<sup>17</sup>, C. R. Burns<sup>18</sup>, G. Clayton<sup>19,20</sup>, M. Dulude<sup>5</sup>, M. Engesser<sup>5</sup>, A. V. Filippenko<sup>21</sup>, S. Gomez<sup>22</sup>, E. Y. Hsiao<sup>2</sup>, T. de Jaeger<sup>23</sup>, J. Johansson<sup>24</sup>, K. Krisciunas<sup>25</sup>, S. Kumar<sup>26</sup>, J. Lu<sup>27</sup>, M. Matsuura<sup>28</sup>, P. A. Mazzali<sup>29,30</sup>, D. Milisavljevic<sup>31</sup>, N. Morrell<sup>32</sup>, R. O'Steen<sup>5</sup>, S. Park<sup>33</sup>, M. M. Phillips<sup>32</sup>, A. P. Ravi<sup>34</sup>, A. Rest<sup>5,35</sup>, J. Rho<sup>36</sup>, N. B. Suntzeff<sup>25</sup>, A. Sarangi<sup>37,38</sup>, N. Smith<sup>39</sup>, M. D. Stritzinger<sup>40</sup>, L. Strolger<sup>5</sup>, T. Szalai<sup>41,42</sup>, T. Temim<sup>43</sup>, S. Tinyanont<sup>44</sup>, S. D. Van Dyk<sup>7</sup>, L. Wang<sup>25</sup>, Q. Wang<sup>45</sup>, R. Wesson<sup>28</sup>, Y. Yang<sup>21,46</sup>, and S. Zsíros<sup>41,47</sup>, Institute for Astronomy, University of Hawai'i at Manoa, 2680 Woodlawn Drive, Hawai'i, HI 96822, USA; kmedler@hawaii.edu
                                                                                                 <sup>2</sup> Department of Physics, Florida State University, Tallahassee, FL 32306, USA
                                                                       <sup>3</sup> Planetary Science Institute, 1700 East Fort Lowell Road, Suite 106, Tucson, AZ 85719-2395, USA

<sup>4</sup> Hamburger Sternwarte, Gojenbergsweg 112, D-21029 Hamburg, Germany
                                                                             <sup>5</sup> Space Telescope Science Institute, 3700 San Martin Drive, Baltimore, MD 21218-2410, USA
                                                                             <sup>6</sup> Institute for Astronomy, University of Hawai'i, 640 N. A'ohoku Place, Hilo, HI 96720, USA
                                                                                                                      Caltech/IPAC, Mailcode 100-22, Pasadena, CA 91125, USA
                                                       <sup>8</sup> Institute of Space Sciences (ICE, CSIC), Campus UAB, Carrer de Can Magrans, s/n, E-08193 Barcelona, Spain
                                                                                                    Institut d'Estudis Espacials de Catalunya (IEEC), E-08034 Barcelona, Spain
                                                                      Center for Cosmology and Astroparticle Physics, The Ohio State University, Columbus, OH, USA

Department of Astronomy, The Ohio State University, Columbus, OH, USA
                                                                                  <sup>12</sup> Ozgrav, School of Physics, The University of Melbourne, Parkville, VIC 3010, Australia
                                                                     <sup>13</sup> Department of Astronomy and Astrophysics, University of California, Santa Cruz, CA 95064, USA
                                               <sup>14</sup> Astrophysics Research Centre, School of Mathematics and Physics, Queen's University Belfast, Belfast BT7 1NN, UK
                                                                     DARK, Niels Bohr Institute, University of Copenhagen, Jagtvej 128, DK-2200 Copenhagen Ø, Denmark
                                                                <sup>16</sup> Institute of Astronomy and Kavli Institute for Cosmology, Madingley Road, Cambridge CB3 0HA, UK
                                                                                          Department of Physics and Astronomy, University of Hawai'i at Hilo, Hilo, HI, USA
                                                             <sup>18</sup> Observatories of the CarnegieInstitution for Science, 813 Santa Barbara Street, Pasadena, CA 91101, USA
                                                                             Department of Physics & Astronomy, Louisiana State University, Baton Rouge, LA 70803, USA

20 Space Science Institute, 4765 Walnut Street, Suite B, Boulder, CO 80301, USA
                                                                                      <sup>21</sup> Department of Astronomy, University of California, Berkeley, CA 94720-3411, USA
                                                <sup>22</sup> Department of Astronomy, The University of Texas at Austin, 2515 Speedway, Stop C1400, Austin, TX 78712, USA
           LPNHE, (CNRS/IN2P3, Sorbonne Université, Université Paris Cité), Laboratoire de Physique Nucléaire et de Hautes Énergies, 75005, Paris, France
                                                              Department of Physics, The Oskar Klein Center, Stockholm University, AlbaNova, 10691 Stockholm, Sweden
    <sup>25</sup> George P. and Cynthia Woods Mitchell Institute for Fundamental Physics and Astronomy, Department of Physics and Astronomy, Texas A&M University,
                                                                                                                                                    College Station, TX 77843, USA
                                                            <sup>26</sup> Department of Astronomy, University of Virginia, 530 McCormick Road, Charlottesville, VA 22904, USA
                                                                              Department of Physics & Astronomy, Michigan State University, East Lansing, MI 48824, USA
 <sup>28</sup> Cardiff Hub for Astrophysical Research and Technology (CHART), School of Physics and Astronomy, Cardiff University, The Parade, Cardiff CF24 3AA, UK
                                                             Astrophysics Research Institute, Liverpool John Moores University, 146 Brownlow Hill, Liverpool L3 5RF, UK
                                                                                 Max-Planck-Institut für Astrophysik, Karl-Schwarzschild Straße 1, 85748 Garching, Germany
                                            <sup>31</sup> Purdue University, Department of Physics and Astronomy, 525 Northwestern Avenue, West Lafayette, IN 4790720, USA
                                                                                              Las Campanas Observatory, Carnegie Observatories, Casilla 601, La Serena, Chile
                                     <sup>33</sup> Department of Physics and Astronomy, Seoul National University, Gwanak-ro 1, Gwanak-gu, Seoul 08826, Republic of Korea
                                                          Department of Physics and Astronomy, University of California, 1 Shields Avenue, Davis, CA 95616-5270, USA
                                                                                  Physics and Astronomy Department, Johns Hopkins University, Baltimore, MD 21218, USA <sup>36</sup> SETI Institute, 339 Bernardo Avenue, Suite 200, Mountain View, CA 94043, USA
                                                                     <sup>37</sup> Indian Institute of Astrophysics, 100 Feet Road, Koramangala, Bengaluru, Karnataka 560034, India
                                                                     <sup>38</sup> DARK, Niels Bohr Institute, University of Copenhagen, Jagtvej 155A, 2200 Copenhagen, Denmark
                                                                                  Steward Observatory, University of Arizona, 933 N. Cherry Street, Tucson, AZ 85721, USA
                                                        Department of Physics and Astronomy, Aarhus University, Ny Munkegade 120, DK-8000 Aarhus C, Denmark
                                                   Department of Experimental Physics, Institute of Physics, University of Szeged, Dóm tér 9, 6720 Szeged, Hungary
                                               <sup>42</sup> MTA-ELTE Lendület "Momentum" Milky Way Research Group, Szent Imre H. st. 112, 9700 Szombathely, Hungary

<sup>43</sup> Princeton University, 4 Ivy Lane, Princeton, NJ 08544, USA
                                                  <sup>44</sup> National Astronomical Research Institute of Thailand, 260 Moo 4, Donkaew, Maerim, Chiang Mai 50180, Thailand
  <sup>45</sup> Department of Physics and Kavli Institute for Astrophysics and Space Research, Massachusetts Institute of Technology, 77 Massachusetts Avenue, Cambridge,
                                                                                                                                                                       MA 02139, USA
```

⁴⁶ Physics Department, Tsinghua University, Beijing 100084, People's Republic of China
 ⁴⁷ HUN-REN CSFK Konkoly Observatory, Konkoly Thege M. ut15-17, Budapest 1121, Hungary
 Received 2025 July 26; revised 2025 September 8; accepted 2025 September 14; published 2025 November 4

Abstract

We present the nebular phase spectroscopic and photometric observations of the nearby hydrogen-rich core-collapse supernova (CCSN) SN 2023ixf, obtained through our JWST programs. These observations, combined with ground-based optical and near-infrared spectra, cover +252.67-719.96 days, creating a comprehensive, panchromatic time-series data set spanning $0.32-30\,\mu\text{m}$. In this second paper of the series, we focus on identifying key spectral emission features and tracking their evolution through the nebular phase. The JWST data reveal hydrogen emission from the Balmer to Humphreys series, as well as prominent forbidden lines from Ne, Ar, Fe, Co, and Ni. NIRSpec observations display strong emission from the first-overtone and fundamental bands of carbon monoxide, which weaken with time as the ejecta cools and dust emission dominates. The spectral energy distribution shows a clear infrared excess emerging by +252.67 days peaking around $10.0\,\mu\text{m}$, with a secondary bump at $18.0\,\mu\text{m}$ developing by +719.96 days. We suggest that this evolution could arise from multiple warm dust components. In upcoming papers in this series, we will present detailed modeling of the molecular and dust properties. Overall, this work provides the community with a unique data set that can be used to advance our understanding of the mid-infrared properties of CCSNe, offering an unprecedented resource for studying their late-time line, molecular, and dust emission.

Unified Astronomy Thesaurus concepts: Type II supernovae (1731); James Webb Space Telescope (2291); Dust formation (2269); Infrared astronomy (786); Core-collapse supernovae (304)

1. Introduction

Core-collapse supernovae (CCSNe), which arise from the collapse of massive stars with zero-age main-sequence mass $M_{\rm ZAMS} \gtrsim 8 \, M_{\odot}$, provide crucial insights into the final stages of stellar evolution (S. J. Smartt et al. 2009). These explosions enrich galaxies with iron-group and α -elements (S. E. Woosley & T. A. Weaver 1995; H.-T. Janka 2012; T. Wang & A. Burrows 2024) and contribute to the formation of galactic dust (E. Dwek et al. 2007; C. Gall et al. 2011). While public, optical, all-sky (e.g., B. J. Shappee et al. 2014; J. L. Tonry et al. 2018), and targeted (e.g., M. Huber et al. 2015; P. J. Groot et al. 2022; M. J. Dyer et al. 2024) surveys now discover thousands of CCSNe annually, the majority of these events are primarily studied in the optical or nearinfrared (NIR), with far fewer observations at the ultraviolet (UV) or mid-infrared (MIR) wavelengths. This observational bias, confined typically to $\sim 0.3-2.5 \,\mu \text{m}$, limits our ability to comprehensively explore the parameter space of the physical conditions and the explosion physics of these objects, as well as their role in galactic chemical and dust enrichment.

The MIR regime, spanning 5–30 μ m, remains relatively underexplored in the study of CCSNe, yet it contains crucial features that are otherwise inaccessible. While strong emission lines are prevalent at all wavelengths, the emission lines located within the optical and NIR can be heavily blended, making species identification and modeling more difficult. In contrast, lines at longer wavelengths ($\geqslant 3 \mu$ m) tend to be significantly less blended, due to reduced overlap of the Doppler broadened lines, allowing for clearer identification and modeling (e.g., A. Jerkstrand et al. 2012; C. Ashall et al. 2024a). Additionally, the IR flux is significantly less affected by extinction from dust along the line of sight, allowing for

Original content from this work may be used under the terms of the Creative Commons Attribution 4.0 licence. Any further distribution of this work must maintain attribution to the author(s) and the title of the work, journal citation and DOI.

more accurate spectroscopic modeling. Several strong C, O, Ne, and Na lines are located in the IR, along with many Fe, Ni, and Co lines, which dominate at late times (e.g., R. Kotak et al. 2005, 2006; A. Jerkstrand et al. 2012). Modeling these IR emission lines provides deeper insight into the progenitor properties than optical modeling alone (e.g., S. E. Woosley & T. A. Weaver 1995; A. Jerkstrand et al. 2012).

MIR observations of SNe offer more than access to unique emission lines; they are essential for tracing dust formation. CCSNe are predicted to contribute significantly to the large dust masses observed in early Universe galaxies (E. Dwek & J. M. Scalo 1980; D. H. Wooden et al. 1993; D. H. Hughes et al. 1997; X. Fan et al. 2003; R. Maiolino et al. 2004; R. Schneider et al. 2004; E. Dwek 2006; C. Gall et al. 2011; D. Watson et al. 2015), as they form dust considerably faster than asymptotic giant branch stars, which dominate dust production in the local Universe (A. S. Ferrarotti & H. P. Gail 2006; R. Valiante et al. 2009; B. F. Williams et al. 2014; J. R. Maund 2017). Both preexisting circumstellar dust heated by the explosion and newly formed dust within the ejecta emit strongly at NIR and MIR wavelengths, making these regimes crucial for identifying and characterizing dust production in SNe (B. Ercolano et al. 2007; R. Kotak et al. 2009; R. Wesson et al. 2015; T. Szalai et al. 2019; A. Sarangi 2022; M. Shahbandeh et al. 2023).

Before the onset of dust formation, CCSNe are expected to synthesize molecules of carbon monoxide (CO) and silicon monoxide (SiO; W. Liu et al. 1992; W. Liu & A. Dalgarno 1994; D. D. Clayton et al. 2001; C. Biscaro & I. Cherchneff 2014; S. Liljegren et al. 2020). Molecules enhance dust formation by acting as nucleation points onto which dust grains can condense (A. Sluder et al. 2018). Additionally, molecules rapidly cool the ejecta to below the dust condensation point, enabling dust formation (W. Liu & A. Dalgarno 1995; S. Liljegren et al. 2020). This cooling happens through reemission via the molecular rovibrational bands, whose spectral signatures are only located at IR wavelengths, with the first overtone of CO ($\Delta v = 2$) located at $\sim 2.3-2.5 \ \mu m$ and the CO and SiO fundamentals ($\Delta v = 1$) located at $\sim 4.3-5.2 \ \mu m$ and $\sim 7.5-9.3 \ \mu m$, respectively (C. P. Snow &

⁴⁸ National Science Foundation Graduate Research Fellow.

⁴⁹ NASA FINESST Future Investigator.

E. K. Rideal 1929; P. D. Singh 1975). The location, formation rate, and total mass of these molecules are highly dependent on the initial mass of the progenitor and offer a unique probe to constrain the progenitor properties and explosion physics (S. E. Woosley et al. 2002; B. Müller et al. 2016).

Several hydrogen-rich Type II CCSNe (SNe II) have displayed molecular features. The CO first overtone was first detected in SN 1987A (R. Catchpole et al. 1987; J. Spyromilio et al. 1988; W. Liu et al. 1992; D. H. Wooden et al. 1993) and later in other events via ground-based (GB) NIR spectroscopy (e.g., J. Spyromilio & B. Leibundgut 1996; C. L. Gerardy et al. 2000; R. Kotak et al. 2005; M. Pozzo et al. 2007; W. P. S. Meikle et al. 2011). Limited MIR coverage has resulted in, with the exception of SN 1987A (D. H. Wooden et al. 1993), only partial observations of the CO fundamental band (D. H. Wooden et al. 1993; R. Kotak et al. 2005; T. Szalai et al. 2011). Finally, the SiO fundamental band, typically emerging several months after the CO (P. F. Roche et al. 1991), has been identified in several late-time MIR spectra (D. H. Wooden et al. 1993; R. Kotak et al. 2006, 2009; T. Szalai et al. 2011; T. Szalai & J. Vinkó 2013).

Once the ejecta is sufficiently cool, $T \leqslant 2000 \, \mathrm{K}$, the formation of fresh dust begins (D. D. Clayton et al. 2001; A. Sarangi & I. Cherchneff 2015; A. Sluder et al. 2018). Signatures of dust typically emerge as an IR excess observed 100 days to a few years after the explosion (P. F. Roche et al. 1989). A time series of NIR and MIR spectroscopy enables detailed tracking of the evolving IR excess and places constraints on key dust properties (e.g., location, composition, and quantity; W. P. S. Meikle et al. 2007; R. Kotak et al. 2009; T. Szalai & J. Vinkó 2013; M. Shahbandeh et al. 2023). While hot dust ($T_{\rm dust} \geqslant 800 \, \mathrm{K}$) can be observed with GB NIR instruments (M. Pozzo et al. 2004; S. Tinyanont et al. 2019; J. Rho et al. 2021; A. P. Ravi et al. 2023; M. Shahbandeh et al. 2023).

The extraordinary capabilities of JWST have dramatically improved our ability to study molecule and dust formation in CCSNe. JWST can simultaneously cover the NIR and MIR regions with the Near-Infrared Spectrograph (NIRSpec; $1.6-5.2~\mu m$) and Mid-Infrared Instrument (MIRI; $4.9-30.0~\mu m$), allowing for comprehensive, simultaneous observations of the CO and SiO emission features, as well as detection of both hot and cool dust in nearby CCSNe (e.g., M. Shahbandeh et al. 2023, 2024; S. Zsíros et al. 2024; G. C. Clayton et al. 2025; M. Shahbandeh et al. 2025).

In this paper, we present JWST spectroscopic and photometric observations of SN 2023ixf spanning approximately +250 to +720 days past explosion. The four epochs of spectroscopic data were obtained as part of our programs JWST-DD-4575 and JWST-GO-5290 (C. Ashall et al. 2023b, 2024b), while the photometric data were acquired through our programs JWST-GO-3921 and JWST-GO-5290 (C. Ashall et al. 2024b; O. Fox et al. 2024). This paper is the second in a series investigating the evolution of SN 2023ixf's panchromatic observations. Here we provide a detailed identification and analysis of emission lines associated with SN 2023ixf and compare the IR data of SN 2023ixf with those of previous SNe II observed during the Spitzer Space Telescope (SST) era and prior.

In Section 2 we present a brief overview of previous work on SN 2023ixf. In Section 3 we describe the GB and JWST observations obtained of SN 2023ixf over the course of 690 days presented in this work. Then, in Section 4 we discuss the evolving panchromatic data of SN 2023ixf, and in Section 5 we examine the key spectral features in the full optical-to-MIR spectrum of SN 2023ixf. In Section 6, we compare the NIR and MIR spectra of SN 2023ixf to those of other SNe II, enabling us to identify spectral differences. The evolving line velocities of several prominent species are discussed in Section 7, followed by a discussion on the location of the dust in the ejecta in Section 8. Finally, we present a summary of the results derived from the panchromatic observations of SN 2023ixf in Section 9. Additional information on the data reduction procedures is provided in Appendix A, and the observation logs and additional GB spectra are presented in Appendix B.

2. Previous Studies on SN 2023ixf

SN 2023ixf, discovered on 2023 May 19.72 (MJD = 60083.73; K. Itagaki 2023), was rapidly classified as a SN II displaying prominent flash ionization features (D. Perley & A. Gal-Yam 2023; E. A. Zimmerman et al. 2024). As one of the closest CCSNe in the past decade, the discovery of SN 2023ixf triggered an unprecedented follow-up campaign across the electromagnetic spectrum ranging from γ -ray to radio, along with multiple multimessenger searches (e.g., E. Berger et al. 2023; K. A. Bostroem et al. 2023; B. W. Grefenstette et al. 2023; D. Guetta et al. 2023; D. Hiramatsu et al. 2023; W. V. Jacobson-Galán et al. 2023; N. Smith et al. 2023; M. Stritzinger et al. 2023; R. S. Teja et al. 2023; J. Thwaites et al. 2023; M. Yamanaka et al. 2023; P. Chandra et al. 2024; G. Martí-Devesa et al. 2024; S. Panjkov et al. 2024; E. Ravensburg et al. 2024; P. Sarmah 2024; A. Singh et al. 2024; S. D. Van Dyk et al. 2024b; Y.-P. Yang et al. 2024; E. A. Zimmerman et al. 2024; A. G. Abac et al. 2025; Y. Iwata et al. 2025; A. J. Nayana et al. 2025), including JWST observations.

Early-time spectra of SN 2023ixf revealed a blue continuum with prominent narrow ($v \lesssim 300 \, \mathrm{km \, s^{-1}}$) emission lines from H and ionized He, C, and N, which persisted for several days (D. Perley & A. Gal-Yam 2023; N. Smith et al. 2023; M. Stritzinger et al. 2023; S. S. Vasylyev et al. 2023; M. Yamanaka et al. 2023; E. A. Zimmerman et al. 2024). These features arise from the ejecta interacting with a dense, asymmetric circumstellar medium (CSM) located $\sim (0.5-1) \times 10^{15} \, \mathrm{cm}$ from the progenitor (K. A. Bostroem et al. 2023; W. V. Jacobson-Galán et al. 2023; S. S. Vasylyev et al. 2023; A. J. Nayana et al. 2025). The spectra of SN 2023ixf evolved over several months, exhibiting characteristics of typical SNe II with a ~ 70 -day-long hydrogen recombination plateau phase (A. Singh et al. 2024; E. A. Zimmerman et al. 2024; W. Zheng et al. 2025).

Pre-explosion multiwavelength imaging at the site of SN 2023ixf indicates a red supergiant progenitor (e.g., J. E. Jencson et al. 2023; C. D. Kilpatrick et al. 2023; Z. Niu et al. 2023; J. L. Pledger & M. M. Shara 2023; M. D. Soraisam et al. 2023; C. L. Ransome et al. 2024). Estimates of the progenitor's mass are bimodal, with models suggesting either a low-mass progenitor ($M_{\rm ZAMS} = 8{-}12\,M_{\odot}$; C. D. Kilpatrick et al. 2023; J. L. Pledger & M. M. Shara 2023; M. C. Bersten et al. 2024; J. M. M. Neustadt et al. 2024; A. Singh et al. 2024;

 Table 1

 Basic Observational Parameters of SN 2023ixf

| Parameter | Value | Source |
|----------------------------|---|----------|
| R.A. | 14 ^h 03 ^m 38 ^s .56 | (1) |
| Decl. | +54°18′41″.94 | (1) |
| $T_{\rm exp}~({ m MJD})$ | 60,082.75 | (2) |
| V _{abs} max (mag) | \sim -18.1 | (3), (4) |
| $V_{\rm app}$ max (mag) | ~11.0 | (3), (5) |
| z | 0.0008 | (6) |
| Distance (Mpc) | 6.9 ± 0.1 | (6) |
| μ (Mpc) | 29.18 ± 0.04 | (6) |
| $E(B-V)_{MW}$ (mag) | 0.0077 ± 0.0002 | (7) |
| $E(B-V)_{\rm Host}$ (mag) | 0.031 ± 0.012 | (8) |

References. (1) TNS; (2) G. Hosseinzadeh et al. (2023); (3) R. S. Teja et al. (2023); (4) W. V. Jacobson-Galán et al. (2023); (5) E. A. Zimmerman et al. (2024); (6) A. G. Riess et al. (2022); (7) E. F. Schlafly & D. P. Finkbeiner (2011); (8) N. Smith et al. (2023).

S. D. Van Dyk et al. 2024b; D. Xiang et al. 2024) or a more massive one ($M_{\rm ZAMS}=17$ –22 M_{\odot} ; J. E. Jencson et al. 2023; C. Liu et al. 2023; Z. Niu et al. 2023; M. D. Soraisam et al. 2023; Y.-J. Qin et al. 2024). Analysis of nebular phase spectra did not decidedly confirm a low- or high-mass progenitor, with mass estimates between $M_{\rm ZAMS}=12$ and 15 M_{\odot} (L. Ferrari et al. 2024; G. Folatelli et al. 2025; A. Kumar et al. 2025; P. D. Michel et al. 2025).

Pre-explosion imaging of SN 2023ixf reveals clear evidence of enhanced mass loss in the final years before explosion (N. Flinner et al. 2023; J. E. Jencson et al. 2023; M. D. Soraisam et al. 2023; J. Zhang et al. 2023; S. Panjkov et al. 2024; Y.-J. Qin et al. 2024; D. Xiang et al. 2024). While mass-loss rates inferred from imaging were modest (10^{-6} to 10^{-4} $M_{\odot}\,\mathrm{yr}^{-1}$), early-time light-curve and spectral modeling suggests a significantly higher rate (10^{-3} to 10^{-2} $M_{\odot}\,\mathrm{yr}^{-1}$), implying a major mass-loss episode shortly before explosion (K. A. Bostroem et al. 2023; W. V. Jacobson-Galán et al. 2023; R. S. Teja et al. 2023). Pre-explosion observations from the SST show a strong IR signal from the progenitor, consistent with heavy obscuration by dust surrounding the progenitor (M. D. Soraisam et al. 2023; T. Szalai & S. V. Van Dyk 2023; S. D. Van Dyk et al. 2024a).

The proximity of SN 2023ixf at \sim 6.9 \pm 0.1 Mpc (A. G. Riess et al. 2022), as well as being one of the brightest SNe observed in decades peaking at V band = \sim 11.0 mag (D. Hiramatsu et al. 2023; R. S. Teja et al. 2023), makes it an ideal candidate for JWST follow-up. An initial JWST observation of SN 2023ixf was obtained during the plateau phase at +33.6 days post-explosion under our project JWST-DD-4722 (C. Ashall et al. 2023a) and is presented in the first paper of this series (J. DerKacy et al. 2025, hereafter Paper I). These observations showed no signs of molecules or dust.

The key properties of SN 2023ixf, such as distance, extinction, and explosion date, adopted throughout this work are listed in Table 1. All phases discussed hereafter are reported in rest-frame days relative to the date of explosion provided in Table 1.

3. Observations

Spectroscopic and photometric JWST observations of SN 2023ixf were obtained at +252.67, +301.72, +373.52, +600.21, and +720 days. The four JWST spectra were

obtained as part of our programs JWST-DD-4575 and JWST-GO-5290 (C. Ashall et al. 2023b, 2024b), and the photometric data were acquired through our programs JWST-GO-3921 and JWST-GO-5290 (C. Ashall et al. 2024b; O. Fox et al. 2024). The stacked photometry from program JWST-GO-3921 obtained at +301.72 days is shown in Figure 1, and all photometric flux and magnitude values from all epochs of SN 2023ixf photometry are given in Table 2. Complimentary GB optical and NIR spectra were also obtained, both to span the epochs between and to coincide with the JWST observations.

The full reduction process for the JWST and GB observations is presented in Appendix A. All observations were reduced using publicly available reduction methods using standard techniques. The JWST data presented in this work were obtained from the Mikulski Archive for Space Telescopes (MAST⁵⁰) at the Space Telescope Science Institute. The specific observations analyzed can be accessed via doi: 10.17909/8kck-p403.

4. Spectral Energy Distribution

Figure 2 presents the $0.32-30.0\,\mu\mathrm{m}$ spectral energy distribution (SED) of SN 2023ixf, spanning from +252.67 to +719.96 days. The SEDs remain relatively flat between 0.32 and $1.2\,\mu\mathrm{m}$ and are dominated by forbidden-line transitions, which evolve in both strength and velocity as different regions of the ejecta become exposed.

During the first two epochs, the SEDs show strong emission from the first-overtone and fundamental rovibrational bands of CO. These emission features weaken substantially by +600.21 days, indicating a decrease in the temperature of the CO region to below 1000 K (S. Liljegren et al. 2020). Future papers in this series will discuss the modeling of the CO features and derived CO properties in SN 2023ixf.

Across the IR regime above $1.5~\mu m$, the flux continuum rises to a peak at $\sim 10.0~\mu m$ in the +252.67-day spectrum, indicating the presence of warm dust. As SN 2023ixf evolves, the IR continuum flux declines in strength alongside the optical, suggesting that the dust mass does not significantly increase during these epochs. By +600.21 days, the $10.0~\mu m$ peak dominates the MIR spectrum over any emission feature, while a secondary peak at $18.0~\mu m$ emerges by +719.96 days. These two MIR features suggest a significant contribution to the flux from Si-rich dust at these later epochs (J. E. Chiar & A. G. G. M. Tielens 2006; J. M. van Breemen et al. 2011; M. Shahbandeh et al. 2023); see Section 8 for further discussion.

5. Identifications of Emission Lines

The identification of spectral features in the late-time spectra of SN 2023ixf provides critical insight into the structure and composition of the ejecta. The dominant features in the +252.67-day optical and GB NIR SEDs of SN 2023ixf include several strong H emission lines, primarily from low-level transitions, as well as prominent O, Mg, and Ca features, as shown in the top panel of Figure 3. Iron-group elements such as Fe, Ni, and Co, along with other α -elements, dominate the emission features in the JWST NIR and MIR regions. As SN 2023ixf evolves, the strength of all emission lines gradually declines as the SN component of the SED fades.

⁵⁰ https://mast.stsci.edu/portal/Mashup/Clients/Mast/Portal.html



Figure 1. A stacked three-color image of the host galaxy spiral arm using the F770W, F1000W, and F1500W MIRI filters from epoch 301.72 days. The location of SN 2023ixf is highlighted by the light-blue circle.

The MIR emission lines become increasingly suppressed owing to the growing contribution from the IR excess that dominates the SEDs, particularly at $t \ge +600$ days.

Below, we highlight the strongest lines of key elemental species identified in the nebular phase spectra from both GB and JWST observations. To support the analysis, we compile spectral lines from previous studies of late-time SNe II spanning the optical, NIR, and MIR regimes (e.g., A. Jerkstrand et al. 2012; S. Davis et al. 2019; M. Shahbandeh et al. 2022). The identified spectral lines appear in Tables 3 and 4.

5.1. Hydrogen

Throughout the evolution of SN 2023ixf, we identify strong hydrogen emission lines from multiple transition series across the optical–MIR spectrum, with several lines displaying strong blending. The observed H lines include the following: Balmer series (n=2)—H α 0.6563 μ m, H β 0.4861 μ m, H γ 0.4340 μ m, and H δ 0.4102 μ m; Paschen series (n=3)—Pa α 1.875 μ m, Pa β 1.282 μ m, Pa γ 1.094 μ m, and Pa δ 1.005 μ m; Brackett series (n=4)—Br α 4.051 μ m, Br β 2.626 μ m, Br γ 2.166 μ m, Br δ 1.944 μ m, and Br ϵ 1.817 μ m; Pfund series (n=5)—Pf α 7.460 μ m, Pf β 4.654 μ m, Pf γ 3.741 μ m, and Pf δ 3.297 μ m; Humphreys series (n=6)—Hu α 12.37 μ m and Hu β 7.503 μ m. We also identify potential emission lines from higher-order transitions, such as H $_{n=9\rightarrow7}$ 11.309 μ m and H $_{n=11\rightarrow8}$ 12.372 μ m.

The emission peaks from the higher-order Balmer series are absent between +252.67 and +373.52 days, as these lines lie within absorption features dominated by heavy elements, particularly Fe, but emerge between +373.52 and +600.21 days. The α through ε transitions of the Paschen, Brackett, Pfund, and Humphreys series are detected in the

+252.67- and +373.53-day spectra. However, at later epochs (+600.21 and +719.96 days), the higher-order transitions, especially the δ and ε lines, become too weak to detect.

The hydrogen lines evolve from the standard P Cygni profile observed at earlier epochs (Paper I) and exhibit three distinct components centered around the rest-frame emission wavelength. The first is a strongly blueshifted peak; the second is a weak, narrow peak located slightly redward of the rest wavelength; and the third is a broad red shoulder. We discuss the origin of these features in detail in Section 7.

5.2. Helium

In the optical, He lines are difficult to identify owing to significant line blending and contamination from other emission features, particularly those from H, Fe, and Na. However, we tentatively identify several weak features commonly associated with He, including He I 0.5876 μ m, He I 0.6678 μ m, and He I 0.7065 μ m. In the NIR we identify the strong He I 1.083 μ m and He I 2.058 μ m.

5.3. Carbon

We identify multiple carbon features, all from neutral C, at C I $0.94~\mu m$, $1.176~\mu m$, $1.181~\mu m$, and $1.454~\mu m$. While the C I $0.94~\mu m$ line blends with nearby O and Fe lines, the other NIR lines are either isolated or blended only with adjacent C lines. Spectral models of other late-time SNe II (A. Jerkstrand et al. 2012) also identify these features, which, together with the prominent CO emission observed in the spectra, support the identification of C in SN 2023ixf.

Table 2
Observation Log of JWST Photometric Imaging Taken through Our Program JWST-GO-3921 (O. Fox et al. 2024) at +301.72 days and Our Program JWST-GO-5290 (C. Ashall et al. 2024b) at +600.21 and +719.96 days

| | Epoch | F770W | F1000W | F1500W | F1800W | F2100W | F2500W |
|--------------------|----------------------------|----------------|-------------------|---|--|---|----------------------------------|
| AB mag. (mag) | 301.72 600.21 | 14.803 ± 0.013 | 14.51 ± 0.008 | 15.023 ± 0.005 15.214 ± 0.001 | 15.180 ± 0.002 | 15.346 ± 0.002 15.274 ± 0.002 | 15.351 ± 0.004 |
| | 719.96 | ••• | ••• | 15.269 ± 0.001 | 14.601 ± 0.001 | 15.283 ± 0.003 | 15.348 ± 0.004 |
| Flux density (mJy) | 301.72 600.21 719.96 | 4.353 ± 0.052 | 5.702 ± 0.042 | 3.555 ± 0.016 2.983 ± 0.003 2.834 ± 0.003 | $$ 3.076 ± 0.005 5.222 ± 0.002 | $\begin{array}{c} 2.64 \pm 0.005 \\ 2.822 \pm 0.004 \\ 2.798 \pm 0.007 \end{array}$ | $ 2.627 \pm 0.01 2.635 \pm 0.01$ |

Note. The epochs are given in days from explosion. Magnitudes and fluxes are not corrected for extinction.

5.4. Oxygen

Throughout the optical and NIR spectra, we identify several emission features associated with oxygen. The strongest O lines in the spectra of SN 2023ixf are the forbidden optical doublet [O I] 0.6300 and 0.6363 μm . In addition to this doublet, we detect several other forbidden and permitted O lines, including [O I] 0.5577 μm , the O I 0.777 μm triplet, [O I] 0.9266 μm , and O I 1.1290 μm . The strength of all O features declines over time, with the NIR lines becoming undetectable between the + 373.52- and + 600.21-day spectra. We discuss the evolution of the [O I] 0.6300 and 0.6363 μm feature in detail in Section 7.

5.5. Neon

A prominent Ne line, associated with the [Ne II] $12.813 \,\mu\text{m}$ transition, appears in the nebular phase MIRI-LRS spectra of SN 2023ixf. No other Ne II lines or other excitation states of Ne are identified in the spectra of SN 2023ixf. This line has also been detected in several MIR observations of other SNe II (R. Kotak et al. 2006; W. P. S. Meikle et al. 2007, 2011).

5.6. Argon

We identify a strong emission feature associated with the [Ar II] $6.985~\mu m$ line. Other lines of Ar, such as [Ar III] $8.991~\mu m$, are not detected in the spectrum, which may indicate that a significant fraction of both noble gases, including Ar and Ne, remain in a neutral state. A similar phenomenon may have also been present in SN 2005af (R. Kotak et al. 2006).

5.7. Calcium

The spectra of SN 2023ixf show multiple Ca lines from both forbidden and permitted transitions. These include the permitted Ca II NIR triplet at 0.8498, 0.8542, and 0.8662 μm ; the Ca II H and K lines at 0.3934 and 0.3969 μm ; and the forbidden [Ca II] 0.7292 and 0.7324 μm lines. As SN 2023ixf evolves, the permitted Ca lines decrease in strength, while the forbidden [Ca II] lines grow more prominent relative to the continuum, consistent with a declining ejecta density.

5.8. Iron

Strong Fe lines appear throughout the late-time optical –MIR spectra of SN 2023ixf. A blend of several Fe II lines are located between $\sim\!0.32$ and 0.5 $\mu\rm m$, including Fe II 0.4352 $\mu\rm m$, Fe II 0.4924 $\mu\rm m$, Fe II 0.5018 $\mu\rm m$, and Fe II 0.5169 $\mu\rm m$. Additional

forbidden and allowed Fe lines are scattered throughout the optical and IR regimes, including [Fe II] 0.7155 μm , [Fe II] 1.279 μm , [Fe II] 1.321 μm , Fe II 1.644 μm , [Fe II] 1.809 μm , Fe II 1.939 μm , Fe II 3.108 μm , Fe II 3.137 μm , and [Fe II] 4.075 μm . We also tentatively identify several weak emission features associated with neutral Fe throughout the spectra of SN 2023ixf, including Fe I 0.5270 μm , Fe I 0.5328 μm , Fe I 0.5587 μm , Fe I 0.7187 μm , and Fe I 1.980 μm .

5.9. Cobalt

We identify several forbidden Co lines in the spectra of SN 2023ixf, including [Co II] 1.019 μm , [Co II] 3.286 μm , [Co II] 10.521 μm , and [Co I] 12.255 μm . We also observe weak features associated with the second ionization state of Co, such as [Co III] 11.886 μm and [Co III] 13.813 μm . However, these features are either very weak relative to the continuum or located near the edge of the instrument's spectral range, where throughput decreases, obfuscating their exact strength and evolution.

5.10. Nickel

In addition to the forbidden Co lines, we identify several forbidden lines from neutral and first ionization state Ni. These include [Ni I] 3.120 μ m, [Ni I] 11.308 μ m, [Ni II] 1.939 μ m, [Ni II] 1.958 μ m, [Ni II] 6.636 μ m, and [Ni II] 10.682 μ m.

5.11. Other Species

We also detect several emission features associated with other elements, including Na (Na I 0.5896 μm , Na I 2.206 μm), Mg (Mg I 0.3832 μm , Mg I 0.457 μm , Mg I 0.518 μm , Mg I 0.517 μm , Mg I 1.488 μm , and Mg I 1.502 μm), Si (Si I 1.203 μm , Si I 1.033 μm , Si I 1.066 μm , [Si I] 1.606 μm , and [Si I] 1.645 μm), S (S I 3.107 μm), Ba (Ba II 0.6142 μm), and Sr (Sr II 1.004 μm , Sr II 1.033 μm , and Sr II 1.092 μm). These lines blend with other emission features, forming shoulders or broad peaks centered between the blended lines.

5.12. Molecules

Several molecular emission features are observed in the NIR/MIR spectra of SN 2023ixf that were not present in the initial JWST data (Paper I). Here we examine the evolution of molecules in SN 2023ixf as it transitions from the SN-dominated phase to the dust-dominated phase, while deferring the spectroscopic modeling of SN 2023ixf's molecular features to a future paper in the series.

Two strong features appear in the spectra of SN 2023ixf, corresponding to the first-overtone and fundamental

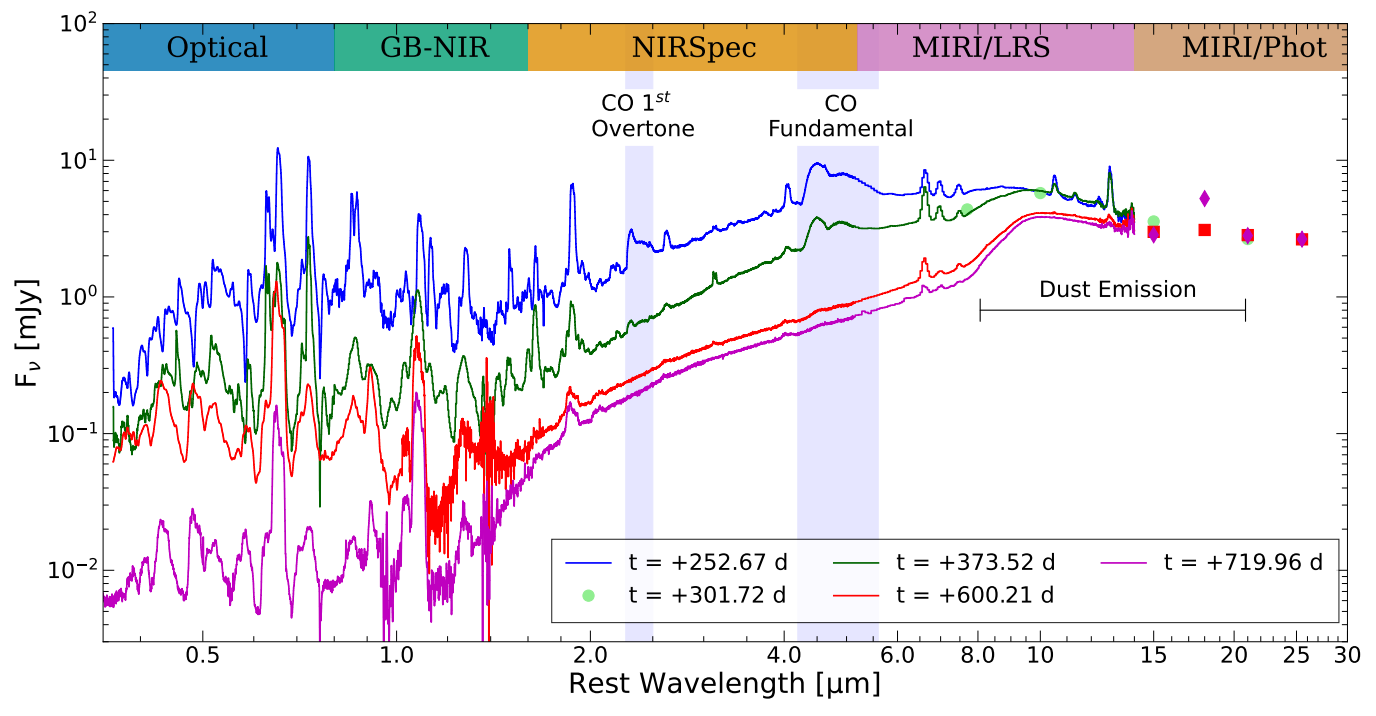


Figure 2. The evolution of the SED covering $0.32-14.0~\mu m$ of SN 2023ixf from +252.67 to +719.96 days post-explosion. Photometry is shown by the colored symbols, at +301.72, +600.21, and +719.96 days. The data have been corrected for extinction and are presented in the rest frame. The SEDs are dominated by a large number of emission lines that decline in strength as SN 2023ixf evolves. CO molecule and dust features are highlighted. In addition, there is a strong IR excess that grows in strength relative to the SN flux at late times.

rovibrational bands of CO. GB NIR observations constrain the emergence of the CO first overtone to between +81 days (G. Li et al. 2025) and +200 days (S. H. Park et al. 2025). In the JWST observations, these features dominate the NIR spectrum of SN 2023ixf from +252.67 to +373.52 days, before fading over the following ~230 days; see the CO regions in Figure 2. By +600.21 days, the CO first overtone completely fades below the continuum level. However, the CO fundamental band remains visible even at +719.96 days, where the broad $\nu=1\rightarrow0$ band head is still detectable above the continuum flux.

Throughout the evolution of SN 2023ixf, both the CO first-overtone and fundamental bands possess distinct broad R- and P-branch emission features, in contrast to the spiky nature of the CO features commonly observed in young stellar objects (e.g., J. D. Ilee et al. 2018; R. Fedriani et al. 2020). These broad shapes arise from the high ejecta velocity blending the higher-order CO transitions into the π_0 and π_1 transitions. The supernova remnant, Cassiopeia A, reveals unique shapes of CO showing R- and P-branches and weak sinusoidal patterns of rovibrational lines with pseudocontinuum underneath, which is attributed to the high-velocity widths of the CO lines (J. Rho et al. 2024). In contrast, the multiple sinusoidal patterns were not observed in SN 2023ixf, as a result of the ejecta possessing a much higher velocity than that of Cassiopeia A.

Emission features in the region between ~ 7.5 and $9.5~\mu m$ are typically associated with the SiO fundamental band (W. Liu & A. Dalgarno 1994; R. Kotak et al. 2006). However, in SN 2023ixf this region does not show the strong emission features expected from SiO vibrational bands at any epoch, instead possessing a rising IR continuum; see Figure 2.

6. Spectral Comparison

To evaluate the uniqueness of SN 2023ixf's infrared spectral features relative to other SNe II, we compare the NIR and MIR spectroscopic observations of SN 2023ixf and several other objects. This comparison reveals both shared and unique features, constraining the structural diversity of these events. As SN 2023ixf evolves, the IR continuum grows stronger and the SN flux fades, drowning out the features from atomic lines. To accurately contrast SN 2023ixf with the other SNe II, we remove the IR continuum by fitting a blackbody at each epoch. A single blackbody, while not physically representative of the underlying physics, works well to capture the shape of the continuum at earlier times, while at later times the dust becomes optically thin, preventing a single blackbody from capturing the full IR continuum shape.

6.1. NIR Comparison

Historically, observations of SNe II in the NIR at late times $(t > 200 \,\mathrm{days})$ have been sparse because of their low luminosities and the lack of telescopes capable of observing these wavelengths. Until recently (M. Shahbandeh et al. 2024; Paper I; E. Baron et al. 2025; T. Mera et al. 2025), SN 1987A was the only SN II with NIR spectroscopic data between 2.5 and $5 \mu m$, obtained from the Kuiper Airborne Observatory (D. H. Wooden et al. 1993). This limited sample prevents robust conclusions regarding the uniqueness of the NIR emission lines and molecular features in SN 2023ixf, especially considering its dusty progenitor, which differs drastically from the blue supergiant progenitor of SN 1987A (R. A. Chevalier & C. Fransson 1987; S. E. Woosley et al. 1988; W. D. Arnett et al. 1989; P. Podsiadlowski 1992). The comparison of the late-time NIR spectra of SN 1987A and SN 2023ixf is shown in the left panel of Figure 4.

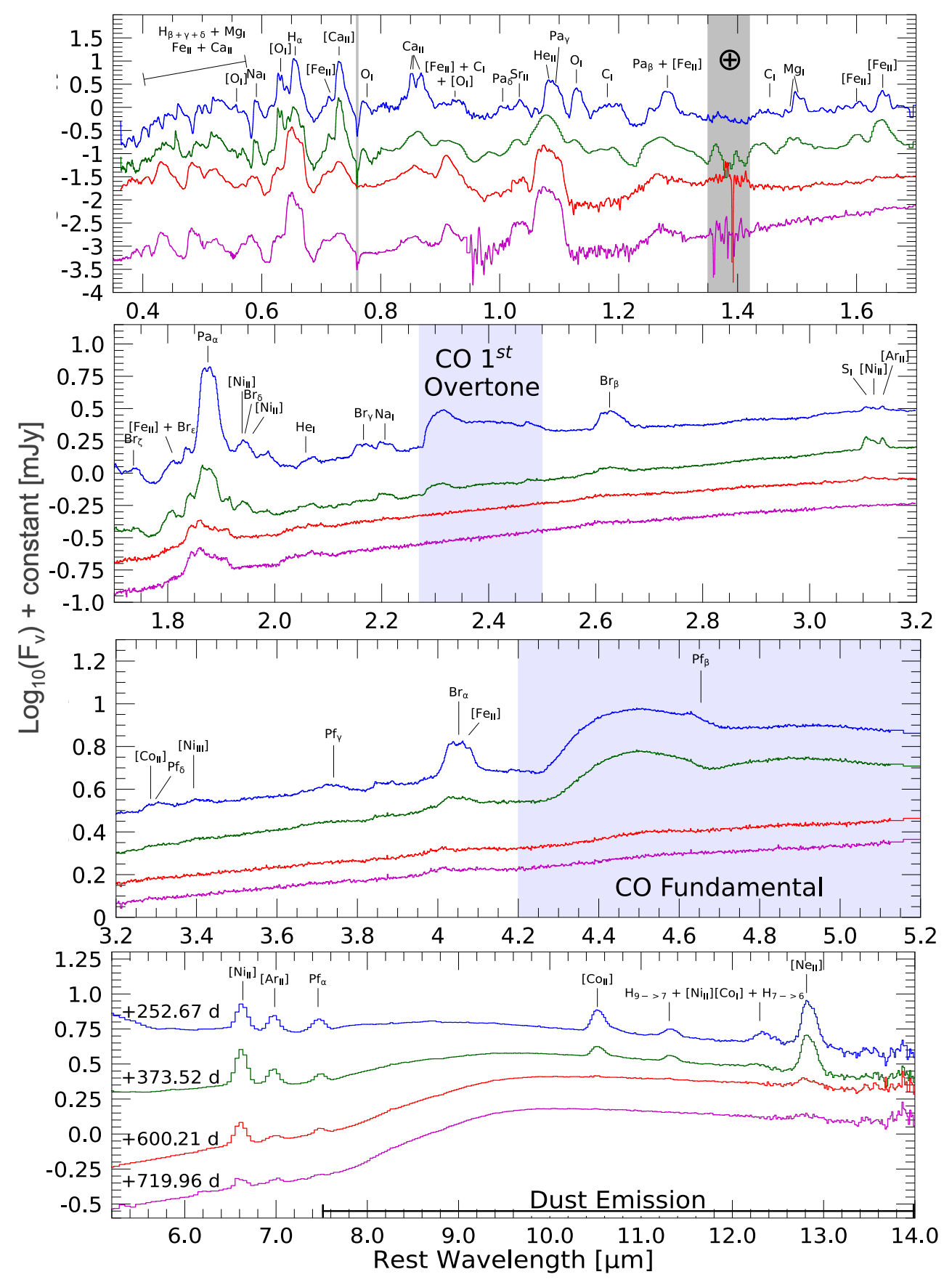


Figure 3. Lines identified within the GB optical and NIR (top row), JWST NIRSpec G235M/F170LP (second row), G395/F290LP (third row), and MIRI (fourth row) spectra of SN 2023ixf at \sim 250 days (blue), \sim 373 days (green), \sim 600 days (red), and \sim 720 days (purple) post-explosion. The spectra have been vertically shifted for clarity. The CO first-overtone and fundamental bands are shown by the shaded blue regions. The full list of identified lines is given in Tables 3 and 4.

Table 3
Identified Nebular Phase Spectral Lines Present in the Optical and Ground-based NIR Spectra

| Ion | Wavelength (µm) | Ion | Wavelength (μm) |
|-------------|-----------------|----------------|-----------------------------|
| | Optical Spectru | m, 0.35–1.0 μm | |
| Mg I | 0.38 | Fe I | 0.5587 |
| Ca II | 0.3934 | Na I | 0.5896 |
| Ca II | 0.3969 | Ba II | 0.6142 |
| $H\delta$ | 0.410.2 | [O I] | 0.6300 |
| $H\gamma$ | 0.4340 | [O I] | 0.6363 |
| Fe II | 0.4352 | α | 0.6563 |
| Mg I] | 0.457 | [Fe II] | 0.7155 |
| $H\beta$ | 0.4861 | Fe I | 0.7187 |
| Fe II | 0.4924 | [Ca II] | 0.7292 |
| Fe II | 0.5018 | [Ca II] | 0.7324 |
| Fe II | 0.5169 | ΟI | 0.777 |
| Mg I | 0.517 | Ca II | 0.8498 |
| Mg I | 0.518 | Ca II | 0.8542 |
| Mg I | 0.518 | Ca II | 0.8662 |
| Fe I | 0.5270 | 0.5270 [O I] | 0.9266 |
| Fe I | 0.5328 | Cï | 0.94 |
| [O I] | 0.5577 | ••• | |
| | GB NIR Spectr | um, 1.0–1.6 μm | |
| Sr II | 1.004 | Si I | 1.203 |
| $Pa\delta$ | 1.005 | [Fe II] | 1.279 |
| [Co II] | 1.019 | $Pa\beta$ | 1.282 |
| Si I | 1.033 | [Fe II] | 1.321 |
| Sr II | 1.033 | CI | 1.454 |
| Si I | 1.066 | Mg I | 1.488 |
| Не І | 1.0830 | Mg I | 1.502 |
| Sr II | 1.092 | [Si I] | 1.606 |
| Pa γ | 1.094 | Fe II | 1.644 |
| ΟÍ | 1.1290 | [Si I] | 1.645 |
| Cı | 1.181 | | |

Even more than a year after explosion, both SN 1987A and SN 2023ixf exhibit several strong H lines throughout the NIR region. The strongest of these lines are the Pa α , Br α , and Br β transitions. Additional weaker spectral features associated with Br γ and Pf β also appear in both data sets, although they are less prominent in SN 2023ixf owing to the strong contribution from the warm dust. A feature located at \sim 3.2 μ m, identified as the [Ni I] 3.120 μ m line in the SN 1987A spectrum (D. H. Wooden et al. 1993), is present in the +415-day spectrum of SN 1987A and in the spectra from +253 to +600 days of SN 2023ixf. While it appears as a single, blended emission feature with a blue shoulder in SN 1987A, the same feature in SN 2023ixf is resolved into a doublepeaked structure. However, the difference in shape between the two SNe is likely due to the higher resolution of the JWST spectra.

In contrast to SN 2023ixf, SN 1987A does not exhibit a rising continuum, instead displaying a relatively flat flux across the NIR region. At >1 yr post-explosion, after removing the infrared excess in SN 2023ixf, both SNe display similar CO fundamental features at \sim 5 μ m and a weak first-overtone feature. Interestingly, the ratio of the CO fundamental peak to the Br α line is much higher in SN 2023ixf than in SN 1987A, and a more prominent Pf β is also observed in SN 1987A; see Figure 4. This difference is particularly pronounced at later times, where the CO fundamental in

Table 4
Identified Nebular Phase Spectral Lines Present in the JWST NIR and MIR Spectra

| Ion | Wavelength (μm) | Ion | Wavelength (μm) |
|----------------------|----------------------|-------------------------|-----------------|
| | | | (μπ) |
| | NIRSpec Spect | trum, 1.6–5.2 μm | |
| Не І | 1.7002 | ${ m Br}eta$ | 2.626 |
| CI | 1.176 | SI | 3.107 |
| [Fe II] | 1.809 | Fe II | 3.108 |
| ${\bf Br} arepsilon$ | 1.817 | [Ni I] | 3.120 |
| $Pa\alpha$ | 1.875 | Ar II | 3.137 |
| Fe II | 1.939 | Fe II | 3.137 |
| [Ni II] | 1.939 | $\mathrm{Pf}\delta$ | 3.297 |
| ${\bf Br}\delta$ | 1.944 | [Co II] | 3.286 |
| [Ni II] | 1.958 | ${ m Pf}\gamma$ | 3.741 |
| Fe I | 1.980 | ${\bf Br} lpha$ | 4.051 |
| Не І | 2.0581 | [Fe II] | 4.075 |
| $\mathbf{Br}\gamma$ | 2.166 | $Pf\beta$ | 4.654 |
| Na I | 2.206 | | |
| | MIRI Spectro | um, 5.2–14 μm | |
| [Ni II] | 6.636 | $H_{n=9\rightarrow7}$ | 11.309 |
| [Ar II] | 6.985 | [Co III] | 11.886 |
| $Pf\alpha$ | 7.460 | [Co I] | 12.255 |
| $Hu\beta$ | 7.503 | $\mathrm{Hu}lpha$ | 12.37 |
| [Co II] | 10.521 | $H_{n=11\rightarrow 8}$ | 12.372 |
| [Ni II] | 10.682 | [Ne II] | 12.813 |
| [Ni I] | 11.308 | [Co III] | 13.813 |

SN 2023ixf is dominant over the ${\rm Br}\alpha$ emission, while in SN 1987A both features are of similar intensity. The disparity in CO and ${\rm Br}\alpha$ intensities may suggest that SN 2023ixf produced significantly more CO than SN 1987A at these epochs. If this is the case, and if we assume that the majority of C and O is bound in CO, then SN 2023ixf would have a larger C/O core than SN 1987A and thus a larger potential initial progenitor mass. However, given the unique status of SN 1987A's progenitor (S. E. Woosley et al. 1988; W. D. Arnett et al. 1989), a large C/O core in SN 2023ixf is only tentatively suggested.

6.2. MIR Comparison

Several SNe II beyond just SN 1987A have been observed at $\lambda > 5~\mu m$ thanks to SST-era programs, including SN 2004dj (T. Szalai et al. 2011), SN 2004et (R. Kotak et al. 2009), and SN 2005af (R. Kotak et al. 2006). The comparison with SN 2023ixf is shown in the right panel of Figure 4. The emission lines of SN 2023ixf appear weaker than those in other SNe II, due to the strong IR excess that enhances the continuum, reducing the relative line strength, especially at longer wavelengths. Once the continuum is subtracted, the line strengths of SN 2023ixf become comparable to the other SNe.

Strong emission features are consistently found across all SNe. These features are associated with Co and Ni lines, as well as the α -elements Ne and Ar. In addition, SN 2023ixf lacks a strong emission of SiO between 7 and 9.5 μ m unlike other SNe, especially SN 1987A. The line strength ratios of the [Ni II] 6.636 μ m, [Ar II] 6.985 μ m, and Pf α 7.460 μ m features of SN 2023ixf are consistent with the other SNe with the exception of SN 2004dj, which possesses a weaker [Ar II] 6.985 μ m feature.

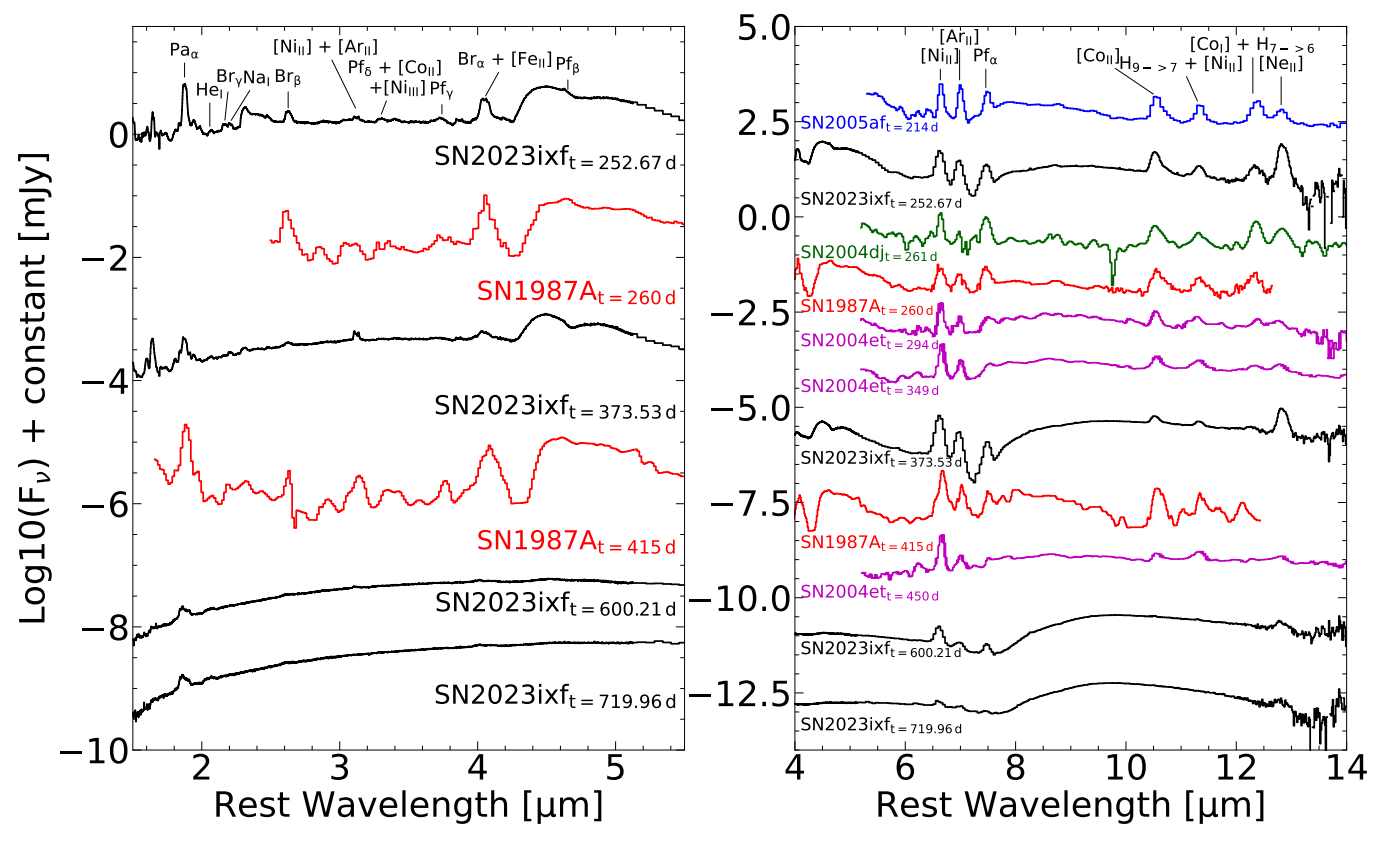


Figure 4. Spectral comparison of SN 2023ixf with several SNe II observed at infrared wavelengths. All spectra have been corrected for redshift and extinction. To aid in comparison, the spectra of SN 2023ixf are continuum subtracted with blackbody functions of 850, 550, 360, and 300 K from the +252.67-, +373.52-, +600.21-, and +719.96-day data, respectively. Left: comparison of the NIR spectra, between 1.5 and 5.5 μ m, of SN 1987A and SN 2023ixf. Right: comparison of the SN 2023ixf MIRI spectra with SN 1987A (D. H. Wooden et al. 1993), SN 2004dj (T. Szalai et al. 2011), SN 2004et (R. Kotak et al. 2009), and SN 2005af (R. Kotak et al. 2006). Both SN 1987A and SN 2004et were digitized from D. H. Wooden et al. (1993) and R. Kotak et al. (2009), respectively.

The [Ne II] 12.813 μ m feature is significantly stronger in SN 2023ixf at all phases relative to the other SNe. While it has been suggested that this line can be powered by interaction (S. Tinyanont et al. 2025), we do not see signatures of interactions such as narrow lines or flat tops in this line, suggesting that the [Ne II] 12.813 μ m originates from within the ejecta. The presence of a strong [Ne II] 12.813 μ m feature indicates that the progenitor of SN 2023ixf possessed a relatively large pre-explosion Ne mass (A. Jerkstrand et al. 2012), which has been associated with a higher progenitor mass (S. E. Woosley & T. A. Weaver 1995; S. E. Woosley et al. 2002). Nebular phase modeling of SN 2004et showed that the [Ni II] 12.729 μ m line becomes significantly stronger as the progenitor mass increases (A. Jerkstrand et al. 2012). Thus, the strong [Ne II] 12.813 μ m line observed in SN 2023ixf suggests a relatively high mass progenitor, potentially larger than the 15 M_{\odot} progenitor of SN 2004et (A. Jerkstrand et al. 2012).

The most notable difference between SN 2023ixf and other SNe in the MIR is its exceptionally strong infrared continuum, with NEOWISE 3.4 and 4.6 μ m photometry identifying SN 2023ixf as one of the brightest SNe II observed in the MIR (S. D. Van Dyk et al. 2024b). This strong infrared continuum dominates the spectra of SN 2023ixf over any other emission feature and is significantly stronger than in any other SN II. SN 2023ixf's infrared excess emerges prior to +252.67 days, several hundred days earlier than the other SNe shown in Figure 4; e.g., SN 2004et developed a strong IR excess after +400 days (R. Kotak et al. 2006, 2009). The

strong IR excess is solely observed in the later epochs, $t \ge +250$ days (Paper I), suggesting that a large amount of dust, either preexisting or freshly formed, is present. While comprehensive modeling of the dust component is left for future papers in this series, we discuss the origins of the infrared excess in Section 8.

7. Line Velocities

The shapes of nebular emission lines are known to encode important information about the physics and evolution of the explosion. Additionally, the shapes of spectral line profiles offer a powerful diagnostic for identifying signatures of newly formed dust.

7.1. Hydrogen Line Diversity

The H profiles in late-time spectra of SNe II have often been used as a key identifier of an asymmetric explosion (D. C. Leonard et al. 2002; V. P. Utrobin & N. N. Chugai 2009) or the formation of dust within the ejecta (D. K. Sahu et al. 2006; R. Kotak et al. 2009; K. Maguire et al. 2010). Newly formed dust attenuates the flux from the receding side of the SN, resulting in a suppression of the redshifted flux and a slightly blueshifted asymmetrical emission peak. This was first identified in SN 1987A (L. B. Lucy et al. 1989) but has since been observed in multiple SNe (L. B. Lucy et al. 1989; R. Kotak et al. 2009; K. Maguire et al. 2010; C. Inserra et al. 2011; N. Smith et al. 2012; M. Stritzinger et al. 2012; C. Gall et al. 2014). Many H

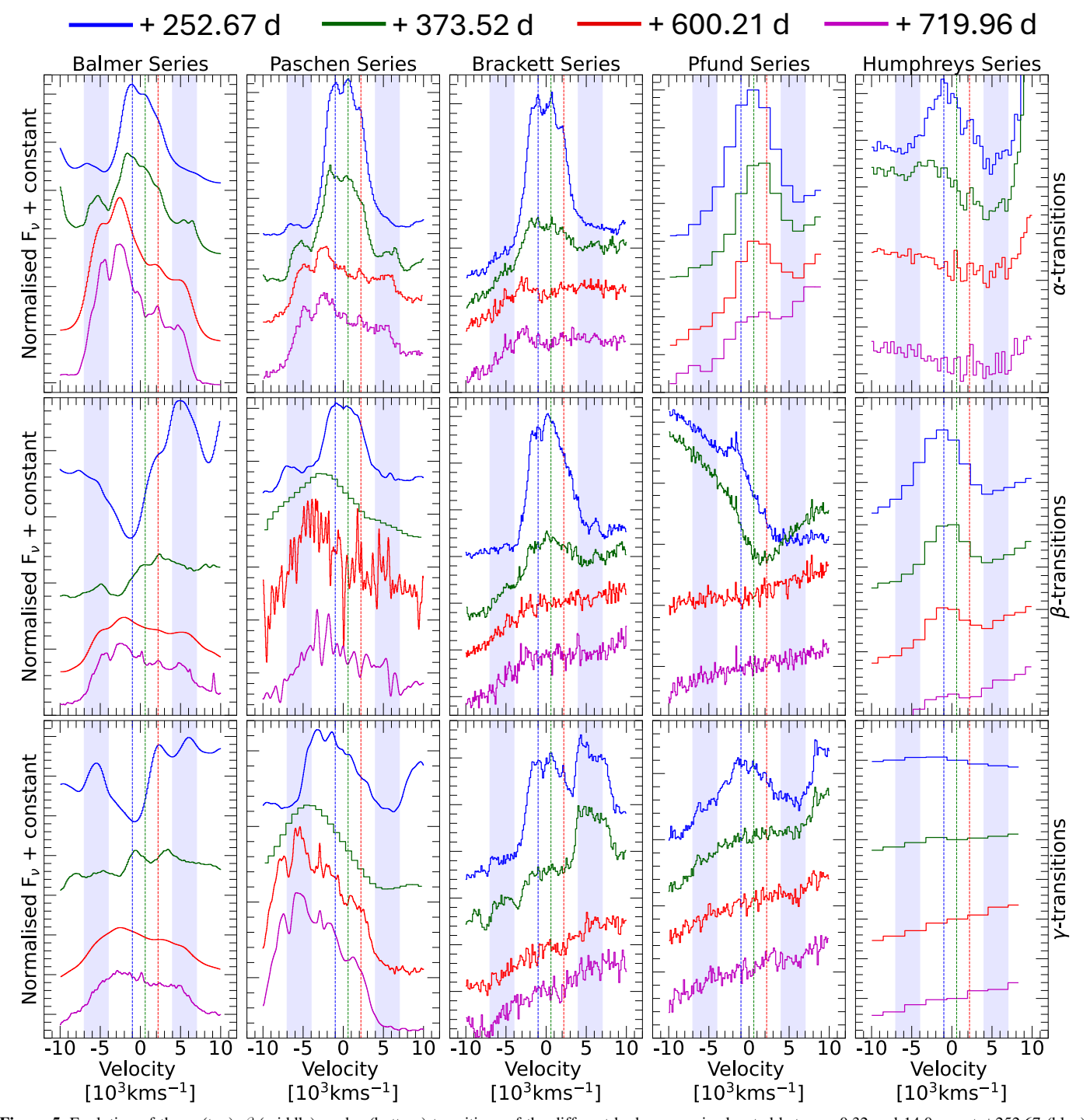


Figure 5. Evolution of the α (top), β (middle), and γ (bottom) transitions of the different hydrogen series located between 0.32 and 14.0 μ m at +252.67 (blue), +373.52 (green), +600.21 (red), and 719.96 days (purple). Several of the isolated hydrogen emission lines, especially the α -transitions, show a triple-peaked profile consisting of a blueshifted peak (-1100 km s⁻¹), a slightly redshifted peak (+500 km s⁻¹), and a strongly redshifted shoulder (+2200 km s⁻¹), shown by the vertical dashed blue, green, and red lines, respectively. Additional high-velocity components (shaded blue regions) emerge between + 252.67 and + 372.53 days, located between \pm 4000 and 8000 km s⁻¹.

lines are clearly present throughout the evolution of SN 2023ixf, and the evolution of the α , β , and γ H transitions from the Balmer to Humphreys series is shown in Figure 5.

Several of the H features seen in the +252.67-day spectrum display a split three-peaked central profile, e.g., $H\alpha$, $Pa\alpha$, $Pa\beta$, $Br\alpha$, $Br\beta$, and $Br\gamma$; see Figure 5. The three peaks correspond to peak shifts of -1100, 600, and $2200 \,\mathrm{km \, s^{-1}}$, identified as the blue, green, and red dashed vertical lines in Figure 5, respectively. These multiple peaks are not always observed in

the higher-order transitions, due to either weak line strengths (e.g., $Pa\gamma$) or blending with emission features from other atomic species or molecules (e.g., $H\beta$ and $Pf\beta$).

The multipeaked emission features are also visible at +600.21 and +719.96 days, although the blueshifted peak has shifted more blueward to $\sim -2500 \, \mathrm{km \, s^{-1}}$, as seen in the $\mathrm{H}\alpha$ and $\mathrm{Pa}\alpha$ profiles in the top row of Figure 5. A similar time-evolving shift is not seen in the two redward peaks. At these later epochs, line blending from other emission features is not

significant; hence, these peaks are visible in the higher-order transitions (see the bottom two spectra of the H β and H γ plots of Figure 5). The origin of the three shifted H α peaks in SN 2023ixf has been associated with strong clumping within ejecta and the surrounding swept-up CSM (e.g., L. Ferrari et al. 2024; A. Singh et al. 2024; A. Kumar et al. 2025).

In addition to the evolving multipeak central emission feature, many of the H profiles exhibit two high-velocity features in the wings of the spectra. These features are boxy in shape and located between ± 4000 and $8000 \, \mathrm{km \, s^{-1}}$, and they are shown by the highlighted blue regions in Figure 5. These structures are most clearly observed in the $\mathrm{H}\alpha$ and $\mathrm{Pa}\alpha$ transitions.

The distinct high-velocity hydrogen features could be produced by the interaction of a fast-moving, asymmetric shock front with a low-density CSM, while the central triple-peaked features can be explained by a slower-moving shock front interacting with dense equatorial CSM (A. Singh et al. 2024; A. Kumar et al. 2025). These complex structures can significantly influence both the molecule and dust formation rates.

7.2. Hydrogen \alpha-series Evolution

The study of the α -series transitions, as the strongest transitions in each H series, allows us to understand properties of the bulk of the H envelope.

7.2.1. Ha Evolution

Examining individual features with high-cadence data may be able to provide additional insight into the physics of the explosion that may be missed with sparsely sampled observations. The evolution of the ${\rm H}\alpha$ feature between 70 and 720 days is shown in Figure 6, with the full optical spectra shown in Appendix B.

Prior to +72.16 days, the ${\rm H}\alpha$ emission feature evolved from a sharp narrow flash ionization emission line (W. V. Jacobson-Galán et al. 2023; E. A. Zimmerman et al. 2024) to a mostly smooth broad P Cygni-like emission profile (A. Singh et al. 2024; W. Zheng et al. 2025; Paper I). The temporal evolution of ${\rm H}\alpha$ in Figure 6 reveals a smooth broad emission peak with an initial blueshift of $\sim\!-1000\,{\rm km\,s^{-1}}$ at +72.16 days that declines to rest velocity by +86.44 days as the ejecta becomes optically thin (J. P. Anderson et al. 2014), which is accompanied by a decline in FWHM from $8000\pm300~{\rm km\,s^{-1}}$ to $5900\pm300~{\rm km\,s^{-1}}$.

Over the \sim 140 days between +86.44 and +212.72 days, the three peaks discussed in Section 7.1 emerge within the H α profile. These three peaks have velocities of \sim -1100, \sim 600, and \sim 2200 km s⁻¹ and are denoted by the blue, green, and red dashed lines in Figure 6, respectively. They show no noticeable velocity evolution between their emergence and the JWST epoch at +252.67 days.

A similar $H\alpha$ evolution has been observed in the nebular phase spectra of several other SNe II (e.g., A. Bevan & M. J. Barlow 2016; M. Niculescu-Duvaz et al. 2022), including SN 1987A (R. Catchpole et al. 1987; R. W. Hanuschik 1988; L. B. Lucy et al. 1989), SN 1999em (D. C. Leonard et al. 2002), and SN 2017gmr (J. E. Andrews et al. 2019). As well as the mechanism discussed in Section 7.1, multiple other origins have been proposed to explain multipeaked $H\alpha$ features.

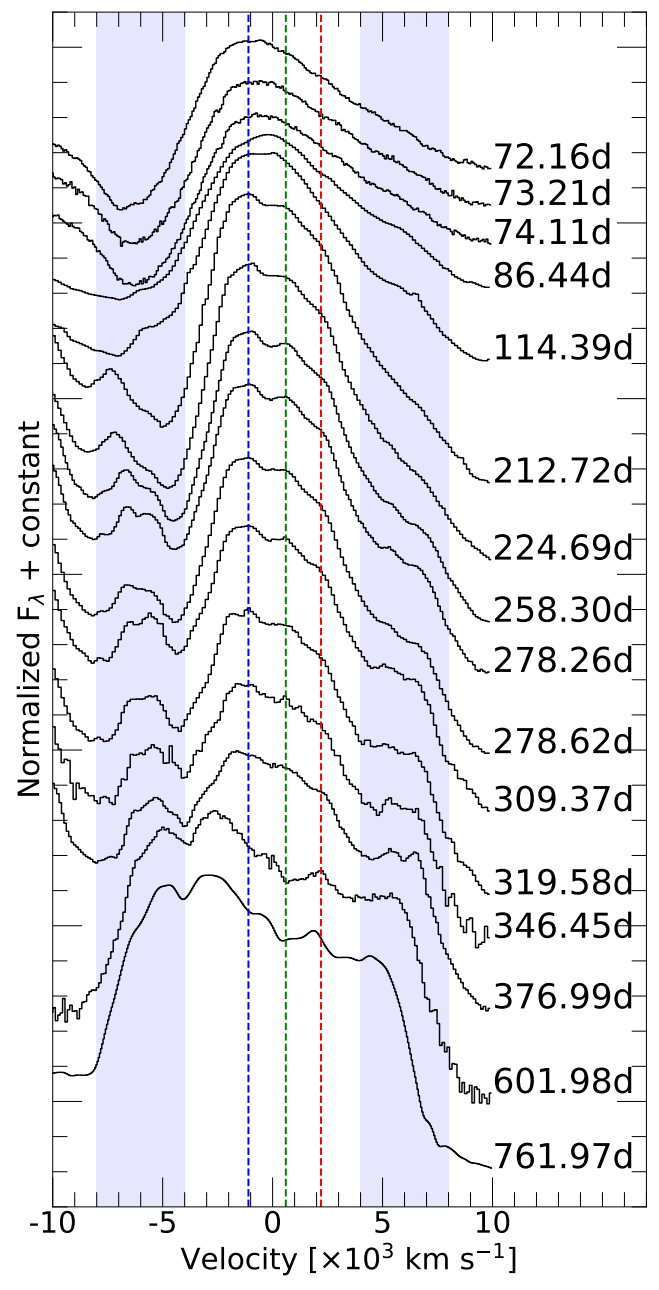


Figure 6. Evolution of the ${\rm H}\alpha$ profile from a blueshifted P Cygni-like feature at +72 days to an asymmetric multipeak feature at +761.97 days, with high-velocity components that emerge around +258.30 days. Earlier spectra are presented in Paper I. All spectra have been corrected for redshift and extinction and have been continuum subtracted. The blue, green, and red vertical lines denote the three shifted peaks located at \sim -1100, \sim 600, and \sim 2200 km s⁻¹, respectively. The blue shaded regions highlight the emerging high-velocity hydrogen features.

Blanketing from an Fe II line has been suggested to cause the asymmetric shape of the $H\alpha$ (P. Hoeflich 1988), with additional line blanketing from the $Br\delta$ and $Br\varepsilon$ lines being invoked to explain the shape of the $Pa\alpha$ line profile. However, this line blanketing cannot be invoked to explain the shape of all the H profiles in SN 2023ixf, as several emission lines are isolated from any lines strong enough to cause blanketing, e.g., $Br\beta$ and $Br\gamma$.

Ejecta asymmetry and the mixing out of 56 Ni have also been invoked to explain sloped H α emission features (A. Elmhamdi et al. 2003). However, significant amounts of 56 Ni mixed

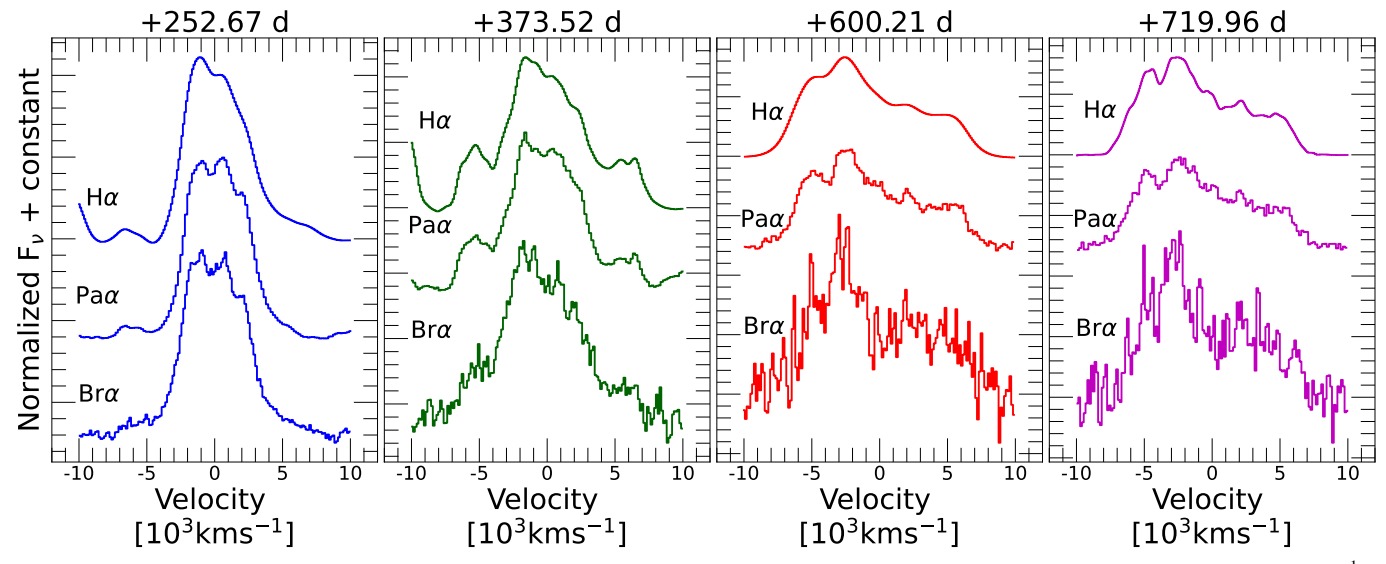


Figure 7. The evolution of the $H\alpha$, $Pa\alpha$, and $Br\alpha$ emission features. All features have been continuum subtracted and normalized to the flux at 0 km s^{-1} . No wavelength-dependent attenuation of the redshifted flux is observed at a given epoch, although a temporal-dependent attenuation is visible.

within the ejecta would result in ionized CO^+ , which appears as an emission peak at 2.26 μ m (J. Spyromilio et al. 1988; C. M. Sharp & P. Hoeflich 1990; J. Rho et al. 2021), which is not observed in SN 2023ixf.

Between +114.39 and +212.72 days, the H α in SN 2023ixf develops a clear high-velocity blueshifted component, with a weaker high-velocity redshifted component emerging by +258.30 days. These features, which are the same as those mentioned in Section 7.1, are highlighted by the shaded blue regions in Figure 6. They are roughly symmetrical around the rest wavelength of H α , with initial velocities of \sim 8000 \pm 500 km s⁻¹ when they first emerge. Thereafter, their velocity declines to \sim 5000 \pm 500 km s⁻¹ by +761.97 days. This is similar to the late-time high-velocity H α profiles seen in SN 1993J (T. Matheson et al. 2000), and as discussed in the previous section, they may be produced by an interaction between a fast-moving shock front and low-density CSM.

Finally, starting at +212.72 days, as H α evolves, the red side of the profile becomes attenuated, creating an asymmetrical, sloped emission peak (see Figure 6). The suppression of the redshifted flux could result from blocking by emission from the receding material. This attenuation may be due to dust formation within the ejecta, as previously suggested for SN 2023ixf (A. Singh et al. 2024).

7.2.2. Panchromatic $H\alpha$ Series

While the study of $H\alpha$ is useful for understanding the evolution of the H envelope, panchromatic coverage of the $H\alpha$ -series transitions enables a joint time- and wavelength-dependent analysis of the splitting and attenuation across multiple features.

The attenuation of the $H\alpha$ feature shown in Figure 6 is also observed in other H emission features; see Figure 5. The majority of these features exhibit strong attenuation of the redside flux relative to the blue side, most prominently in the α -transitions. The normalized, continuum-subtracted emission features of the $H\alpha$, $Pa\alpha$, and $Br\alpha$ transitions for each JWST epoch are shown in Figure 7. For each emission feature, a flat continuum was fit across the bottom to remove the

contribution from the IR excess, which significantly affects the shape of the redder emission lines.

All of the features exhibit similar structures, consisting of multiple peaks as highlighted in the previous sections. Additionally, the shapes of the profiles at each epoch are remarkably consistent, with attenuation of the red side of the features that increases over time. This wavelength-dependent analysis allows us to test for dust attenuation, which one might think would typically affect the bluer emission features over the redder ones. In SN 2023ixf, we observe the same level of attenuation at a given epoch for all the features shown in Figure 7, regardless of wavelength. The absence of wavelength-dependent attenuation suggests that the shape of these features is not solely due to dust attenuation. However, as we discuss further in Section 8.3, this in fact is heavily influenced by grain size and dust composition.

7.3. Oxygen and Calcium Velocity Evolution

The optical lines of O show a systematic blueshift of $\sim\!-1300\pm500\,\mbox{km\,s}^{-1}$ from the point at which they first appear in the spectra of SN 2023ixf (see Figure 8). The blueshift in the optical O profiles is consistent with the shift observed in the H lines. However, the NIR O I 1.1290 μm feature does not show a similar blueshift, which may indicate that these lines form in different regions of the ejecta.

The optical [Ca II] 0.7292, 0.7324 μm doublet and the Ca II NIR triplet exhibit no significant shifts from their rest wavelengths at any epoch shown in Figure 8, or in other published observations (A. Singh et al. 2024; G. Li et al. 2025). However, the Ca features also develop a red-side attenuation similar to the hydrogen emission features. This was also observed by A. Singh et al. (2024).

7.4. Neon and Argon Velocity Evolution

The MIR contains lines from elements that lack emission features in shorter-wavelength regions (e.g., Ar and Ne). The JWST spectra of SN 2023ixf show two strong lines associated with Ar and Ne, located at 6.985 and 12.813 μ m, respectively. The velocity evolution of these lines is presented in Figure 9.

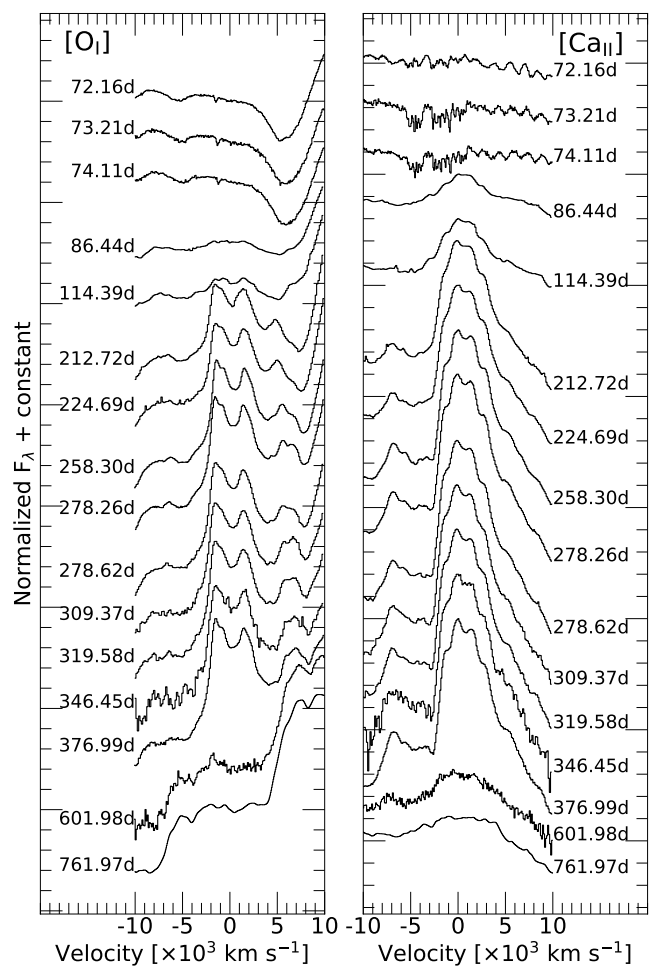


Figure 8. Spectral evolution of the [O I] 0.6300, 0.6363 μm doublet and [Ca II] 0.7292, 0.7324 μm doublet. The features are plotted in velocity space relative to the rest-frame wavelengths of the [O I] 0.6300 μm and [Ca II] 0.7292 μm lines, respectively. The [O I] 0.6300, 0.6363 μm features show a significant blueshift of \sim 1300 \pm 500 km s⁻¹, similar to the blue peak observed in the split H emission peak, while the [Ca II] 0.7292 0.7324 μm doublet remains centered at the rest wavelength. The difference in the location of the peaks suggests that the O and Ca are located in drastically different regions of the SN ejecta.

The [Ar II] 6.985 μ m features maintain roughly the same shape and are centered around $(0.0\pm0.5)\times10^3$ km s⁻¹ in all epochs except at +713.73 days, where the [Ar II] 6.985 μ m line shows a slight redshift of ~2000 km s⁻¹ in its central peak; see the bottom panel left panel of Figure 9.

In the first two epochs, [Ne II] 12.813 μ m displays a slightly asymmetric emission feature with an enhanced flux shoulder at \sim 1900 \pm 500 km s⁻¹. This can be explained by the blending of the [Ne II] line with a weaker emission feature, which is supported by the shape of [Ne II] 12.813 μ m at + 600.21 and +713.13 days, where a second peak emerges coincident with the location of the red shoulder; see Figure 9.

7.5. Nickel and Cobalt Velocity Evolution

Deeper within the ejecta, Ni and Co form during the explosive nuclear burning of core collapse. The [Co II] $10.521~\mu m$ line, shown in Figure 9, exhibits nearly perfect symmetry around $0~km~s^{-1}$ throughout SN 2023ixf's evolution, suggesting that cobalt is centrally located within the ejecta with minimal mixing into the outer regions.

In contrast, the velocity evolution of the [Ni II] $6.636\,\mu\mathrm{m}$ line, also shown in Figure 9, reveals a tentative blueshift in its emission peak of $\sim\!1000\pm500\,\mathrm{km\,s^{-1}}$, evolving to $\sim\!2000-3000\,\mathrm{km\,s^{-1}}$ at $+719.96\,\mathrm{days}$. The initial blueshift of the [Ni II] $6.636\,\mu\mathrm{m}$ line mirrors the peak velocity seen in the blue peak of the H lines in Figure 5 and the [O I] $0.6300, 0.6363\,\mu\mathrm{m}$ lines. However, the shift in [Ni II] $6.636\,\mu\mathrm{m}$ is likely caused by the low spectral resolution and is not intrinsic to the elemental distribution in the explosion.

7.6. Ejecta Geometry and Clumping

Several emission lines in SN 2023ixf, including those from H and O, exhibit blueshifted peaks. While some of this shift, especially in the H emission features, could be explained by the presence of dust-obscuring emission from the receding ejecta (see Section 8), the observed asymmetries also point to an intrinsically aspherical explosion geometry or clumping within the ejecta (A. Singh et al. 2024).

Aspherical ejecta are common for SNe II and can naturally arise from jet-driven explosion mechanisms (e.g., A. Khokhlov & P. Höflich 2001; L. Scheck et al. 2006; M. Modjaz et al. 2008; S. Taubenberger et al. 2009; D. Milisavljevic et al. 2010; J. E. Andrews et al. 2011b; H.-T. Janka et al. 2016; M. A. Tucker et al. 2024). In such scenarios, a significant fraction of the ejecta moves toward the observer, resulting in a net blueshift. The observed flux asymmetry around the rest wavelengths of the lines provides a direct probe of the degree of asymmetry in the explosion.

In SN 2023ixf the shifts in emission peaks we observe could also result from an asymmetric distribution of $^{56}\rm Ni$ within the ejecta (C. L. Gerardy et al. 2000; V. P. Utrobin & N. N. Chugai 2017; S. Bose et al. 2019). In this scenario, uneven heating of the surrounding O-rich material by $^{56}\rm Ni$ would lead to asymmetric oxygen emission features (C. L. Gerardy et al. 2000; K. Maeda et al. 2008). However, we disfavor this interpretation owing to the symmetric profile of the [Co II] 10.521 $\mu\rm m$ line and the absence of CO+, which forms through mixing between the CO- and $^{56}\rm Ni$ -rich regions.

The discrepancy between the blueshifted O lines and the symmetrical line profiles observed in other species, such as Ca, Ar, and Co, could also be explained as a combination of a high-density clump, or torus, of O-rich material interacting with the equatorial dense CSM moving along our line of sight and a bulk ejecta distributed around 0 km s⁻¹ (Q. Fang et al. 2024; L. Ferrari et al. 2024; A. Kumar et al. 2025). This ejecta structure was first observed in SN 1987A (H. Li & R. McCray 1992) and has since been identified in several other SNe (D. Milisavljevic et al. 2010; H. Kuncarayakti et al. 2020; Q. Fang et al. 2022).

Although an aspherical explosion geometry explains the systematic blueshifts observed in the O emission profiles, it does not account for the evolving morphology of the H-series lines, which have a time-dependent attenuation of the red-side flux and multiple peaks. This requires interaction with a clumpy CSM and possibly dust formation in the ejecta. Overall, while detailed modeling is necessary to fully distinguish between each proposed scenario, we provide our favored explanation of the atomic line structure of SN 2023ixf in Figure 10.

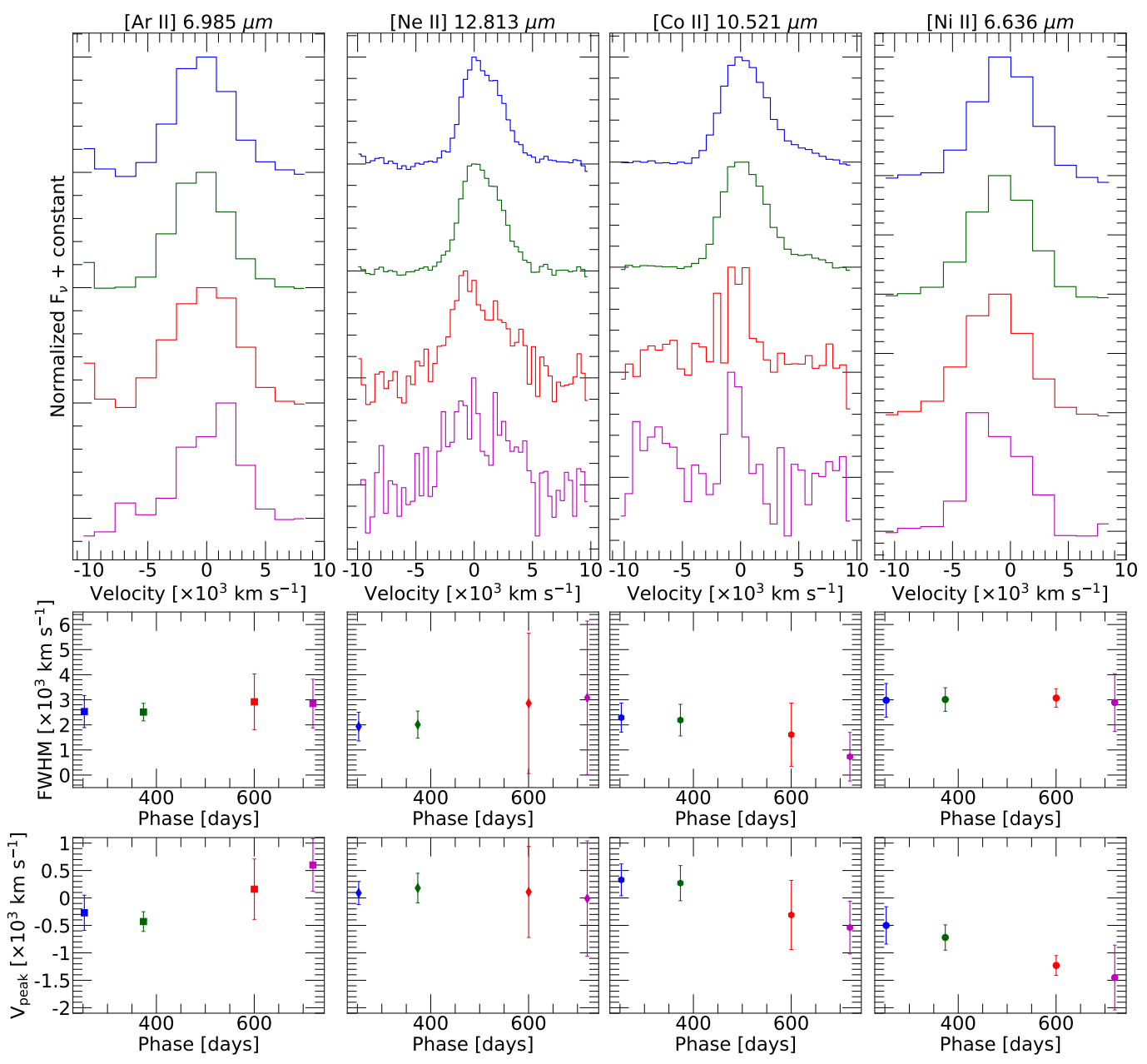


Figure 9. Velocity evolution of [Ni II] $6.636 \, \mu m$, [Ar II] $6.985 \, \mu m$, [Co II] $10.521 \, \mu m$, and [Ne II] $12.813 \, \mu m$. While the neon, argon, and cobalt lines are centered around $0 \, km \, s^{-1}$, the nickel emission feature is blueshifted by $\sim 1000 \pm 500 \, km \, s^{-1}$ at all epochs. All emission features have been corrected by removing a linear continuum across the bottom of the features to remove the influence of the IR excess, especially at late times, when the lines are weaker. The FWHM and peak velocity determined by Gaussian fits are shown in the middle and bottom rows, respectively.

8. Origin of the Dust Emission

While it is clear that dust plays a significant role in the evolution of SN 2023ixf, determining the origin of this dust is not straightforward. As noted in Section 4, the +252.67-day spectrum of SN 2023ixf shows a strong, featureless IR excess. By +373.52 days, a broad continuum feature develops around $10.0~\mu m$, which remains present in subsequent epochs. The IR continuum of SN 2023ixf does not change again significantly until +719.96 days, when a second peak emerges at $\sim 18.0~\mu m$. These peaks, at ~ 10.0 and $\sim 18.0~\mu m$, are indicative of silicate-rich dust (M. Shahbandeh et al. 2023).

The evolving SED of SN 2023ixf can be explained by several possible sources of dust (see Figure 5 in A. Sarangi et al. 2018), including (1) preexisting dust in the CSM located

beyond the explosion's evaporation radius (M. F. Bode & A. Evans 1980; E. Dwek 1983; J. E. Andrews et al. 2011a), (2) freshly formed dust in the cool dense shell (CDS) between the forward and reverse shocks (M. Pozzo et al. 2004; N. Smith et al. 2008; C. Gall et al. 2014), and (3) newly condensed dust within the SN ejecta itself (R. Kotak et al. 2005; J. E. Andrews et al. 2011b; T. Szalai & J. Vinkó 2013). Although determining the precise dust properties of SN 2023ixf requires detailed modeling, which we reserved for a future paper in this series, we discuss the plausibility of each dust source below.

8.1. Preexisting CSM Dust

The first option is that the IR excess originates from preexisting dust located outside the evaporation radius of the

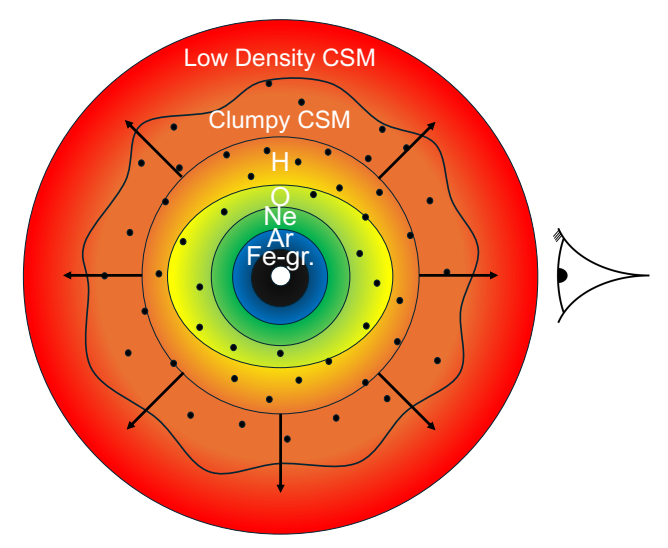


Figure 10. Structure of SN 2023ixf and its surrounding CSM. Black circles indicate clumps within the dense CSM, as well as H- and O-rich ejecta. The elemental distribution explains the observed line features in H, O, Ne, Ar, Co, and Ni. Variations in the hydrogen velocities and spectral bumps arise from interactions of H-rich ejecta with both low-density and clumpy CSM. The blueshifted O peaks are best explained by asymmetric O-rich ejecta or a massive O-rich clump along the line of sight. A jet, oriented perpendicular to the observer's view (eye symbol, right), could also naturally account for the asymmetric distribution; however, more detailed modeling is required to establish its presence.

explosion. This dust is heated by the shock breakout emission and, as the dust evolves, transitions from optically thick to optically thin, causing the shape of the IR emission to change (A. Sarangi et al. 2018; M. Shahbandeh et al. 2023). This dust would reside in the CSM of the progenitor, or the interaction region between the CSM and the ISM (P. Dragulin & P. Hoeflich 2016).

At +252.67 days, the infrared continuum is well approximated by a blackbody with a temperature of 688 K, which is well below the evaporation temperature for both carbonates and silicates; hence, it is produced from warm dust. Assuming an optically thick and spherical dust distribution, a dust temperature of 688 K would correspond to a radius of $r_{\rm dust} = 2.2 \times 10^{16}$ cm. A similar value, $r_{\rm dust} \sim 1.6 \times 10^{16}$ cm, was suggested from a 700 K blackbody fit to the 3.4 μ m NEOWISE photometry at +212 days (S. D. Van Dyk et al. 2024b). For SNe II, the typical photospheric radius is $(1-10)\times 10^{14}$ cm (e.g., P. Hoeflich 1988; L. Dessart & D. J. Hillier 2005), with photospheric temperatures of 5000 –10,000 K. New dust forms once the ejecta drops below the evaporation temperature, and it would reside close to the photosphere, assuming $T_{\rm dust} \propto \sqrt{R_{\rm ph}}$, while heated dust should be located farther out, $\approx 100R_{\rm ph}$.

Moreover, the CSM distance derived from the X-ray emission, $<7 \times 10^{15}$ cm, is likely produced in the low-density region (100–10,000 times the ISM density) and by the interaction between the reverse shock and the wind-like CSM (R. Margutti et al. 2012; P. Dragulin & P. Hoeflich 2016; B. W. Grefenstette et al. 2023; S. Panjkov et al. 2024; A. J. Nayana et al. 2025). High-velocity ejecta from the SNe (\gtrsim 30,000 km s⁻¹) would traverse the CSM with minimal deceleration, reaching radii of \sim 2 × 10¹⁶ cm within a few months. This rapid interaction would be expected to cause dust evaporation, producing an infrared component near the dust

sublimation temperature ($T \gtrsim 2000~\rm K$), in contrast to the warm dust (688 K) temperatures that are actually observed. Given this, the ejecta is unlikely to have reached the dust region, even by $+250~\rm days$, placing the dust at distances similar to the estimate from the infrared continuum. In reality, the CSM is likely not a spherical shell and is likely clumpy, meaning that $2.2 \times 10^{16}~\rm cm$ should only be taken as a strict lower limit. An asymmetric clumpy CSM is also supported by the X-ray and radio observations, which require significant clumping to find agreement in the derived X-ray and radio CSM density profiles (S. Panjkov et al. 2024; A. J. Nayana et al. 2025). Future, detailed analysis is required to determine the exact location and nature of the dust.

8.2. Cold Dense Shell Dust

The second mechanism involves the formation of dust within the CDS produced in the post-shocked CSM. As the forward shock moves through the surrounding CSM and the reverse shock traverses into the inner ejecta, material is built up, shocked, and heated. This postshock gas then rapidly cools, through a combination of free-free and molecular/ atomic line cooling, forming a CDS sufficiently cool and dense enough to facilitate the formation of dust (A. Sarangi et al. 2018). This dust is heated by ionizing photons from the forward shock, with dust above 2000 K rapidly subliming after formation. It may be assumed that, given the temperature dependence, the CDS is unlikely to be the cause of the initial IR excess observed at t < 250 days, as the heating from the forward shock would inhibit dust formation (A. Sarangi et al. 2018). At later times, as the shock luminosity declines, the gas temperature in the CDS becomes conducive to dust formation. However, for CDS dust to account for the observed attenuated line profiles (if they are not produced from a geometry effect), it would need to be mixed into the ejecta.

8.3. Ejecta Dust

The third location for dust formation is within the expanding ejecta interior to the reverse shock. Dust can be formed within the ejecta once the temperature drops below the condensation temperature. This is facilitated by emission from molecular rovibrational bands, features that are observed in the spectra as early as +252.67 days. While ejecta dust could explain the late-time IR excess, the ejecta temperature would be too high at earlier phases to allow for dust formation (A. Singh et al. 2024). For example, in some instances, in situ dust formation is not expected to occur until at least 450 days after the explosion (A. Sarangi 2022).

One hallmark of dust formation in the ejecta is the attenuation of the red side of optical emission features (C. Gall et al. 2014). This is clearly observed in the $H\alpha$ series and [Ca II] 0.7292, 0.7324 μ m line profiles. For SN 2023ixf, we also observe time-dependent attenuated profiles in the $Pa\alpha$ and $Br\alpha$ features, suggesting that this is not a wavelength-dependent effect (at least between 0.5 and 4 μ m). While one might expect dust blocking to show a strong wavelength dependence, given the blue Rayleigh scattering, previous studies have examined this issue. L. B. Lucy et al. (1989) considered the effects of scattering via dust albedo and concluded that, for SN 1987A, scattering was negligible. They also inferred a grain size of $a \le 0.05 \ \mu$ m. In the DAMOCLES

code (A. Bevan & M. J. Barlow 2016; A. Bevan 2018), scattering is modeled using the Henyey-Greenstein phase function, and no significant variations are observed across the Balmer lines (A. Bevan & M. J. Barlow 2016, see their Figure 9). While we acknowledge the possibility of dust producing a wavelength-dependent blocking effect, the literature does not find a strong wavelength dependence for the lines we observe in SN 2023ixf, and we defer further conclusions to future work in the series.

8.4. The Full Picture

In reality, a combination of dust formation processes may be required to explain the observed properties of SN 2023ixf. The strong IR excess at +252.67 suggests the presence of dust in either the CSM or the CDS. Given the dusty nature of the progenitor, significant heating of preexisting dust in the CSM might be expected.

The evolution of the line profiles may also indicate that some dust may be present within the ejecta. This dust may form as the ejecta cools below the condensation temperature or originate in the CDS and subsequently mix into the ejecta (A. Bevan et al. 2019; A. Singh et al. 2024). The latter scenario implies a clumpy dust structure. However, these profiles could also be produced by geometry effects, and detailed modeling is needed to distinguish between these possibilities.

Overall, we tentatively suggest that the IR excess in SN 2023ixf results from a combination of preexisting dust in the CDS or in the CSM, which dominates at early times, and newly formed dust, which becomes more prominent at later epochs. This newly formed dust likely originates from within the ejecta, in a clumpy CDS that mixes into the ejecta, or a combination of both. We will examine this in more detail in the next papers of the series.

9. Conclusions

In this paper we present the panchromatic data set of SN 2023ixf spanning from 0.32 to 30.0 μ m between +252.67 and +719.96 days past explosion, with optical data spanning from +72.16 to +224.69 days. This is the most complete JWST time series of a SN II to date. In this second paper of our series, we concentrate on presenting this exquisite data set, as well as identifying the predominant spectral lines and molecular bands that form in the ejecta. The data presented here were obtained from the NIRSpec, MIRI-LRS, and MIRI-imager instruments and supplemented with data from a variety of GB telescopes, allowing us to construct 0.32–30 μ m panchromatic SEDs. The main results from our work are as follows:

- 1. The JWST spectra of SN 2023ixf reveal a rich array of atomic species, including rare members of the hydrogen Brackett, Pfund, and Humphreys series, as well as forbidden lines from Co, Ni, Fe, Ne, and Ar. C, O, Mg, Na, and Ca lines are also present in SN 2023ixf at shorter wavelengths (see Section 5).
- 2. SN 2023ixf shows significant features of CO formation, visible by the first-overtone and fundamental rovibrational bands, which were not present in the earlier JWST spectrum (Paper I). While the first overtone fades by +600.21 days, the fundamental band remains detectable

- at all epochs, indicating that the CO region is dropping in temperature below 1000 K (see Section 5.12).
- 3. The splitting of late-time H lines from the Balmer, Paschen, and Brackett series into multiple features suggests that SN 2023ixf was likely an asymmetric explosion with a two-component clumpy CSM. Additional high-velocity features, linked to an aspherical shock front, are also observed (see Section 7.2).
- 4. Several emission lines in SN 2023ixf (e.g., H and O) exhibit blueshifted peaks, consistent with an aspherical, clumpy explosion geometry. A high-density clumpy or asymmetric distribution of O-rich material expanding along the line of sight, combined with spherical Ca-, Arand ⁵⁶Ni-rich regions, explains the observed blueshifts and the lack of velocity shifts in Ca, Ar, and Co lines (see Section 7.6).
- 5. The SED of SN 2023ixf shows a time-evolving IR dust component that emerges by +252.67 days, with distinct features indicative of Si-rich dust appearing at $10~\mu m$ by +373.52 days and $18~\mu m$ by +719.96 days (see Section 4).
- 6. The initial (+252.67 days) featureless IR continuum may be explained by the presence of preexisting dust located outside the evaporation radius of SN 2023ixf, which is consistent with the dusty nature of the RSG progenitor star (see Section 8).
- 7. The time-evolving obscuration of the red side of $H\alpha$, $Pa\alpha$, $Br\alpha$, and $[Ca II] 0.7292 0.7324 <math>\mu m$ may be explained by the start of dust formation, or as a result of an aspherical explosion geometry. If the attenuation is caused by dust, it may have formed within the ejecta or in a clumpy, cold, dense shell that mixes into the ejecta (see Section 8).
- 8. We tentatively suggest that the IR excess observed in SN 2023ixf arises from a combination of preexisting, likely Si-rich, dust in the CSM or CDS, dominant at early times, and newly formed dust either within the ejecta or in a clumpy CDS that mixes into the ejecta (see Section 8). However, detailed models are required to explore this further.

While it is beyond the scope of this paper to determine the exact grain size, mass, and location of the dust, such early emission of dust suggests that some amount of preexisting dust ejected by the RSG progenitor can survive within the CSM and survive the forward shock of the explosion. However, disentangling the exact location of the dust (CSM vs. CDS vs. ejecta) is left for a more detailed analysis, which will be presented in future papers of this series.

Overall, JWST has allowed the MIR region of the electromagnetic spectrum to be explored in unprecedented detail. In this paper, the second in the series, we have presented nebular phase panchromatic data of SN 2023ixf and demonstrated how these data can be used to explore the line formation processes in the various wavelength regions in the ejecta. In future papers, we will focus on both molecule and dust modeling of the respective features, determining their properties, mass, and location, and examine how this links to the progenitor system. SN 2023ixf is becoming one of the best-observed SNe II to date, and future scheduled JWST and GB observations will ensure that this truly amazing data set continues to improve.

Acknowledgments

K.M., E.B., C.A., J.D., M.S., P.H., and A.V.F. acknowledge support from NASA grants JWST-GO-02114, JWST-GO-02122, JWST-GO-04522, JWST-GO-04217, JWST-GO-04436, JWST-GO-03726, JWST-GO-05057, JWST-GO-05290, JWST-GO-06023, JWST-GO-06677, JWST-GO-06213, and JWST-GO-06583. Support for program Nos. 2114, 2122, 3726, 4217, 4436, 4522, 5057, 6023, 6213, 6583, and 6677 were provided by NASA through a grant from the Space Telescope Science Institute, which is operated by the Association of Universities for Research in Astronomy, Inc., under NASA contract NAS 5-03127.

Some of this material is based on work supported by the National Science Foundation Graduate Research Fellowship Program under grant Nos. 1842402 and 2236415 and NSF award AST-230639 to P.H. Any opinions, findings, conclusions, or recommendations expressed in this material are those of the author(s) and do not necessarily reflect the views of the National Science Foundation.

D.O.J. acknowledges support from NSF grants AST-2407632 and AST-2429450, NASA grant 80NSSC24M0023, and HST/JWST grants HST-GO-17128.028, HST-GO-16269.012, and JWST-GO-05324.031, awarded by the Space Telescope Science Institute (STScI), which is operated by the Association of Universities for Research in Astronomy, Inc., for NASA, under contract NAS5-26555.

M.D.S. is funded by the Independent Research Fund Denmark (IRFD, grant No. 10.46540/2032-00022B) and by an Aarhus University Research Foundation Nova project (AUFF-E-2023-9-28).

A.V.F. is grateful to the Christopher R. Redlich Fund for additional support.

L.G. acknowledges financial support from AGAUR, CSIC, MCIN, and AEI 10.13039/501100011033 under projects PID2023-151307NB-I00, PIE 20215AT016, CEX2020-001058-M, ILINK23001, COOPB2304, and 2021-SGR-01270.

Based on observations made with the Gran Telescopio Canarias (GTC), installed at the Spanish Observatorio del Roque de los Muchachos of the Instituto de Astrofísica de Canarias, on the island of La Palma.

The Shappee group at the University of Hawai'i is supported with funds from NSF (grants AST-2407205) and NASA (grants HST-GO-17087, 80NSSC24K0521, 80NSSC24K0490, 80NSSC23K1431).

J.T.H. was supported by NASA grant 80NSSC23K1431.

Parts of this research were supported by the Australian Research Council Centre of Excellence for Gravitational Wave Discovery (OzGrav), through project No. CE230100016.

S.Z. received support from the NKFIH OTKA K142534 grant.

Parts of this research were supported by the Australian Research Council Centre of Excellence for Gravitational Wave Discovery (OzGrav), through project No. CE230100016.

D.M. acknowledges support from the National Science Foundation (NSF) through grants PHY-2209451 and AST-2206532.

M.M. and R.W. acknowledge support from the STFC Consolidated grant (ST/W000830/1).

R.W. acknowledges support from the European Research Council (ERC) Advanced Grant SNDUST 694520.

Facilities: JWST (NIRSpec and MIRI), ING:Newton (IDS), IRFT (Spex), GTC (OSIRIS+ and EMIR), Keck:I (LRIS), Keck:II (NIRES), UH:2.2m (SNIFS).

Software: Astropy (Astropy Collaboration et al. 2013, 2018, 2022), Dust-extinction (K. D. Gordon et al. 2023; K. Gordon 2023), JWST reduction notebooks (D. Law et al. 2025), JWST Science Calibration Pipeline (ver. 1.18.0; (H. Bushouse et al. 2022)), Matplotlib (J. D. Hunter 2007), Numpy (C. R. Harris et al. 2020), SciPy (P. Virtanen et al. 2020), Sextractor (A. Burrow et al. 2020).

Data Availability

All spectra presented in this paper are available at the Weizmann Interactive Supernova Data Repository (WISeREP;⁵¹ O. Yaron & A. Gal-Yam 2012).

Appendix A Observations and Data Reductions

Below we discuss the reduction procedure for the JWST NIRSpec and MIRI-LRS observations, as well as GB optical and NIR spectra.

A.1. JWST MIRI Imaging

We obtained three epochs of JWST MIRI imaging of SN 2023ixf through two of our programs: JWST-GO-3921 (O. Fox et al. 2024) and JWST-GO-5290 (C. Ashall et al. 2024b). The first epoch, acquired by JWST-GO-3921 at +301.72 days post-explosion, includes imaging in the F770W, F1000W, F1500W, and F2100W filters. The second and third epochs, obtained by JWST-GO-5290 at +600.21 and +719.96 days, respectively, use the same instrument with the F1500W, F1800W, F2100W, and F2500W filters. A stacked color image from the first epoch is presented in Figure 1. We perform point-spread function (PSF) photometry using a custom Python notebook built on the WebbPSF-based space phot package (M. D. Perrin et al. 2014).⁵² We select the PSF width to minimize residuals in the fit, accounting for the expected wavelength-dependent broadening. For each dither in which SN 2023ixf is detected, we average the individual flux measurements and estimate the photometric uncertainty from the standard deviation across the dithers. The AB magnitudes and corresponding flux densities (in mJy) for all filters and epochs are summarized in Table 2.

A.2. JWST Spectroscopy

We obtained JWST spectra of SN 2023ixf on 2024 January 26, 2024 May 26, 2025 January 8, and 2025 May 2 using NIRSpec (P. Jakobsen et al. 2022; T. Böker et al. 2023) and MIRI in Low Resolution Spectroscopy mode (MIRI/LRS; S. Kendrew et al. 2015). We reduced all spectra using the standard NIRSpec fixed-slit and MIRI LRS-slit Jupyter notebooks (D. Law et al. 2025), with version 1.18.0 of the JWST calibration pipeline (H. Bushouse et al. 2022), JWST Build version 11.3, and Calibration Reference Data System file jwst_1364.pmap.

⁵¹ https://www.wiserep.org/

 $^{^{52}}$ https://github.com/orifox/psf_phot/blob/main/space_phot/MIRI/miri_1028.ipynb

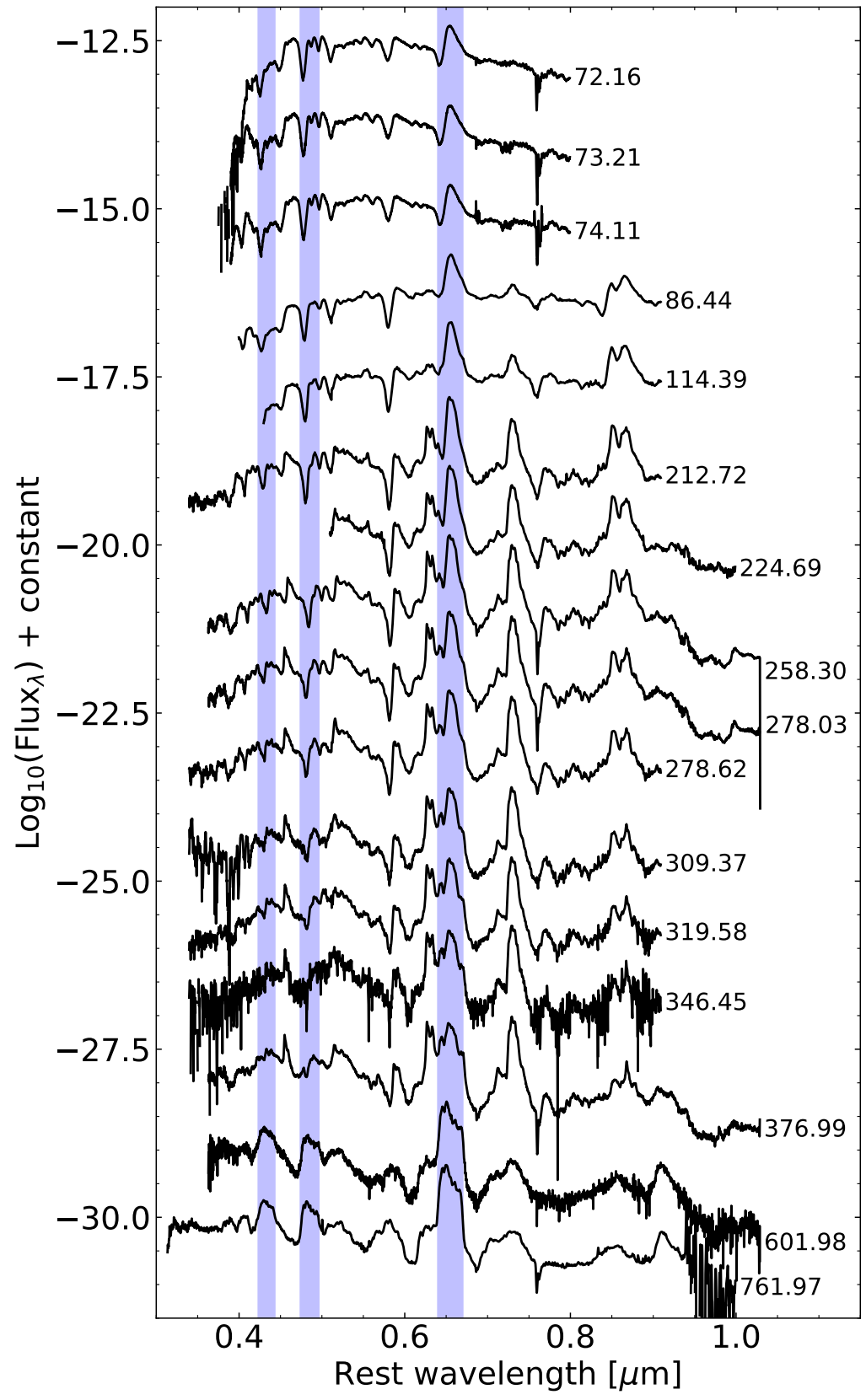


Figure A1. The optical spectral time series of SN 2023ixf used in this work. All spectra have been corrected for redshift and extinction. The phase relative to the explosion date is given for each spectrum on the right. The emission regions of the $H\alpha$, $H\beta$, and $H\gamma$ lines are highlighted by the blue regions.

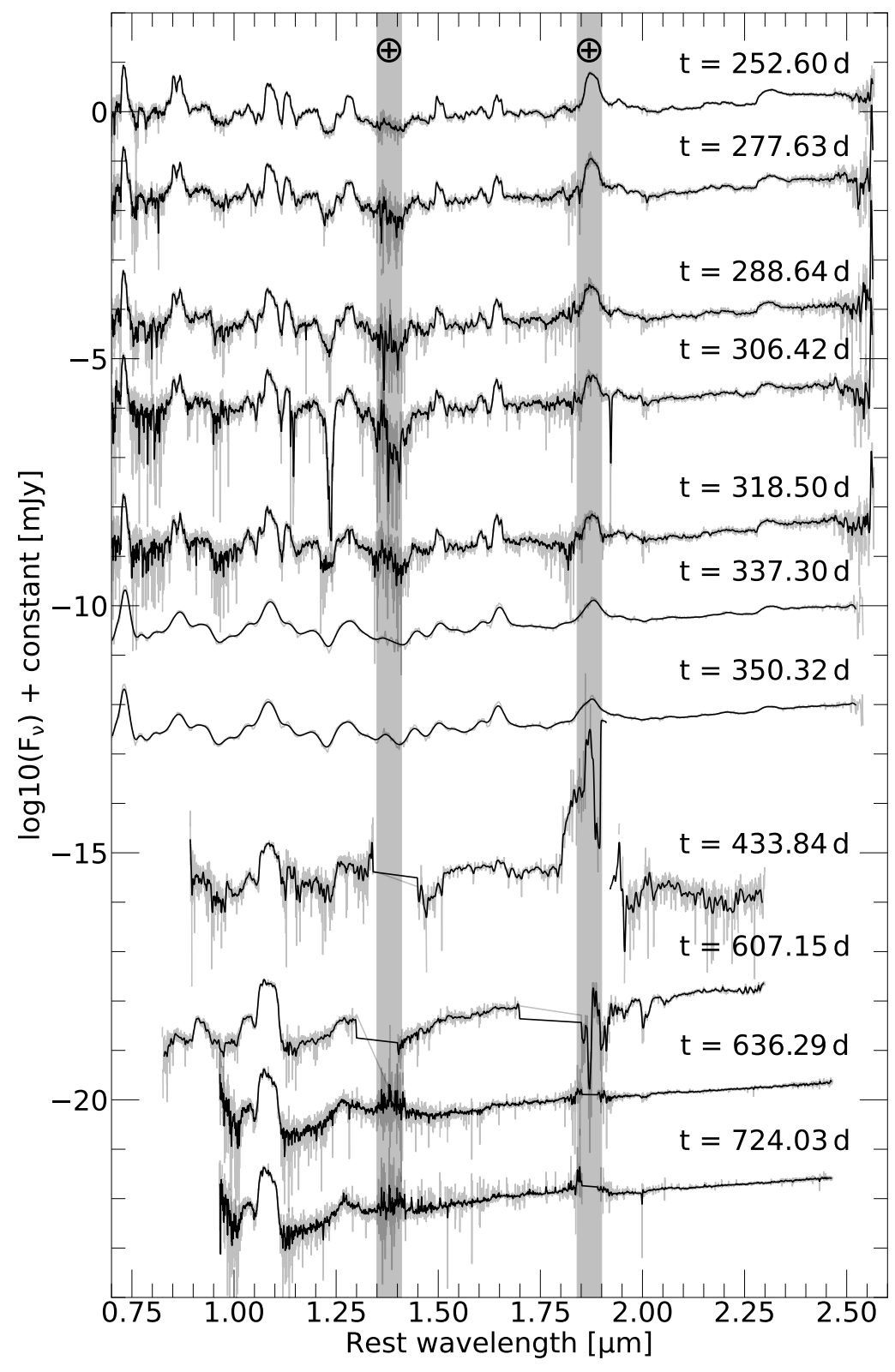


Figure A2. IRTF/SpeX and Keck/NIRES spectra of SN 2023ixf between 250 and 725 days. The telluric regions are highlighted by the gray regions. As SN 2023ixf evolved, the CO first-overtone feature, $2.2-2.5~\mu m$, declined in strength, and a strong IR excess developed in the NIR continuum above $\sim 1.2~\mu m$, corresponding to hot dust.

A.2.1. NIRSpec

The NIRSpec observations used the F170LP/G235M and F290LP/G395M filter/grating combinations, covering the $1.66-3.07~\mu m$ and $2.87-5.10~\mu m$ ranges, respectively. The

observations employed the S400A1 subarray and a three-pointnod dither pattern. Exposure times were increased over time to account for the fading SN flux, ensuring a high enough signalto-noise ratio (SNR) to trace the evolution of the CO first overtone, fundamental band, and other spectral features. Full details of the NIRSpec configuration are provided in Appendix A.2.

We modified the standard reduction parameters to include a scaling factor in the outlier_detection step during stage 3 spectroscopic processing. This scale value varies between 0 and 1.2 to minimize noise spikes, caused by bad pixels when combining the three dithers, while preserving the source flux. All reduction stages—stage 1 detector processing, stage 2 image processing, stage 2 spectroscopic processing, and stage 3 spectroscopic processing—were run on uncalibrated NIRSpec images downloaded from MAST.

A.2.2. MIRI-LRS

The MIRI observations utilized the LRS mode, covering a wavelength range of ~ 5 –14 μm (S. Kendrew et al. 2015). All epochs were taken using the full subarray, the FASTR1 readout pattern, and the along-slit-nod dither pattern. Exposure times were increased to account for the declining flux of SN 2023ixf. Details on the exposure times and readout settings for each epoch are provided in Appendix B. We use the standard reduction parameters to run all processing stages on the uncalibrated MIRI-LRS images downloaded from MAST.

A.3. Ground-based Spectroscopy

The GB optical and NIR observations were obtained as close to contemporaneous with the JWST observations as possible to ensure no significant evolution of the emission features between the observations. Details on the optical and GB NIR observations are given in Appendix B, while the full optical and GB NIR spectra are presented in Figures A1 and A2, respectively.

A.3.1. Optical

Optical spectra were obtained at similar epochs to the JWST spectral observations using the Optical System for Imaging and low-Intermediate-Resolution Integrated Spectroscopy (OSIRIS+) on the 10.4 m Gran Telescopio Canarias (GTC; P. Alvarez et al. 1998). We reduce the GTC data using standard procedures, including bias subtraction, flat-fielding of the two-dimensional images, wavelength calibration of the extracted spectrum from arc lamp exposures, and the removal and correction of telluric features and cosmic rays. Multiple exposures were obtained in the R1000B and R1000R filters and median-combined to increase the SNR of the optical spectra. An additional optical spectrum was obtained using the 10 m Keck I telescope with the Low-resolution Imaging Spectrometer (LRIS; J. B. Oke et al. 1995; J. K. McCarthy et al. 1998; C. Rockosi et al. 2010) to complement the +713day JWST spectra. The LRIS observations used the 600/4000 grism on the blue side and the 400/8500 grating on the red side. Multiple images were obtained with exposure times of 1800 and 900 s for the blue and red arms, respectively. We reduce the individual arms separately using the automated spectroscopic reduction code Pypeit, 53 version 1.17.3.

Optical spectra, covering 72–279 days, were taken on the University of Hawai'i 88-inch telescope (UH88) located on Maunakea using the SuperNova Integral Field Spectrograph (SNIFS; G. Aldering et al. 2002; B. Lantz et al. 2004) through the Spectroscopic Classification of Astronomical Transients (SCAT; M. A. Tucker et al. 2022) survey, as well as on the Intermediate Dispersion Spectrograph (IDS⁵⁴) mounted on the Isaac Newton Telescope (INT). We reduce the SNIFS spectra using the procedure detailed in M. A. Tucker et al. (2022) and the IDS spectra via the standard reduction pipeline (T. E. Müller Bravo 2023).

A.3.2. Near-infrared

NIR spectra covering $\sim\!\!0.7-2.5\,\mu m$ were obtained by the Hawai'i Infrared Supernova Study (K. Medler et al. 2025) using SpeX (J. T. Rayner et al. 2003) on the 3.0 m NASA Infrared Telescope Facility (IRTF) and the Near-Infrared Echellette Spectrometer (NIRES; J. C. Wilson et al. 2004) on the 10 m Keck II telescope.

The IRTF spectra were taken in ShortXD mode, with a slit size of $0\rlap.{''}8\rlap/{''} \times 15\rlap/{''}$ using ABBA dithering. We reduce these observations with the Spextool software package (M. C. Cushing et al. 2004) applying telluric corrections that use an AV0 star that was at a similar air mass to SN 2023ixf. More details on the reduction procedure can be found in K. Medler et al. (2025), W. B. Hoogendam et al. (2025b), and W. B. Hoogendam et al. (2025a).

The NIRES spectra were also taken using ABBA dither patterns with 300 s individual exposure times. We reduce these Keck II/NIRES observations in a similar manner to the IRTF/SpeX observations, using the Keck II/NIRES version of the Spextool package (for more information, see K. Medler et al. 2025).

Additional spectra were obtained with GTC using the Espectrógrafo Multiobjeto Infra-Rojo spectroscope (EMIR; F. Garzón et al. 2022) and the Gemini Near IR Spectrograph (GNIRS; M. Dubbeldam et al. 2000) mounted on Gemini-North. We reduce the EMIR observations with our own pipeline based on PyEmir (S. Pascual et al. 2010; N. Cardiel et al. 2019; S. Pascual et al. 2019), while the GNIRS spectrum is reduced using Pypeit using an AV0 star as the telluric standard following the procedures described in W. B. Hoogendam et al. (2025a, 2025b).

Appendix B Observation Log and GB Spectra

Here we provide detailed logs of all of the observations, analyses, and results used in this work. The JWST and GB optical and NIR spectral observations are presented in Tables B1 and B2, respectively.

https://pypeit.readthedocs.io/en/1.17.3/index.html

⁵⁴ https://www.ing.iac.es/Astronomy/telescopes/int/

 Table B1

 Log of JWST Spectroscopic Observations

| Parameter | Visit 2 | Visit 3 | Visit 4 | Visit 5 |
|---------------------------|---------------------|---------------------------|---------------------|---------------------|
| | | NIRSpec Spectral Observa | tions | |
| Mode | Fixed Slit | Fixed Slit | Fixed Slit | Fixed Slit |
| Slit | S400A1 | S400A1 | S400A1 | S400A1 |
| Grating/filter | G235M-F170LP/G395M- | G235M-F170LP/G395M- | G235M-F170LP/G395M- | G235M-F170LP/G395M- |
| | F290LP | F290LP | F290LP | F290LP |
| Exp time/dither (s) | 63.90/63.90 | 157.38/157.38 | 163.61/126.22 | 163.61/126.22 |
| Phase (days) | 252.66/252.65 | 373.52/373.51 | 600.21/600.20 | 722.90/722.98 |
| $T_{\rm obs} ({ m MJD})$ | 60335.61/60335.60 | 60456.57/60456.56 | 60683.44/60683.42 | 60806.23/60806.22 |
| | | MIRI Spectral Observation | ons | |
| Mode | LRS | LRS | LRS | LRS |
| Exp time/dither (s) | 255.30 | 505.06 | 277.50 | 277.50 |
| Phase (days) | 252.69 | 373.54 | 600.23 | 714.08 |
| $T_{\rm obs}$ (MJD) | 60335.64 | 60456.58 | 60683.46 | 714.08 |

Table B2
Log of GB Optical and NIR Spectra of SN 2023ixf Obtained between +250 and +765 days

| | | and 1703 days | |
|--------------------|--------------|---------------------------|----------------------|
| Obs. Date (MJD) | Phase (days) | Exp. Time (s) | Telescope/Instrument |
| | | Optical Spectra | |
| 60154.97 | 72.16 | 600 | INT/IDS |
| 60155.02 | 73.21 | 600 | INT/IDS |
| 60156.92 | 74.11 | 2×600 | INT/IDS |
| 60169.26 | 86.44 | 2×1800 | UH88/SNIFS |
| 60197.23 | 114.39 | 1800 | UH88/SNIFS |
| 60295.64 | 212.72 | 1800 | UH88/SNIFS |
| 60307.62 | 224.69 | 1800 | UH88/SNIFS |
| 60340 | 258.39 | 2×900 | GTC/OSIRIS+ |
| 60361 | 278.03 | 4×450 | GTC/OSIRIS+ |
| 60361.59 | 278.62 | 2×1800 | UH88/SNIFS |
| 60392.37 | 309.37 | 1800/1200 | UH88/SNIFS |
| 60402.59 | 319.58 | 1800 | UH88/SNIFS |
| 60429.48 | 346.45 | 1800 | UH88/SNIFS |
| 60459 | 375.95 | 2×600 | GTC/OSIRIS+ |
| 60685 | 601.77 | 4×500 | GTC/OSIRIS+ |
| 60845.33 | 761.97 | $6\times1800/12\times900$ | Keck I/LRIS |
| | | NIR Spectra | |
| 60335.55 | 252.60 | 44 × 120 | IRTF/SpeX |
| 60360.60 | 277.63 | 14×120 | IRTF/SpeX |
| 60371.62 | 288.64 | 8 × 120 | IRTF/SpeX |
| 60389.42 | 306.42 | 18×120 | IRTF/SpeX |
| 60401.50 | 318.50 | 30×120 | IRTF/SpeX |
| 60420.32 | 337.30 | 14×120^{a} | IRTF/SpeX |
| 60433.35 | 350.32 | 10×120^{a} | IRTF/SpeX |
| 60516.94 | 433.84 | 121 | GTC/EMIR |
| 60690.39 | 607.15 | 20×300.0 | Gemini-N/GNIRS |
| 60719.55 | 636.29 | 12×300.0 | Keck II/NIRES |
| 60807.36 | 724.03 | 22×300.0 | Keck II/NIRES |

Notes. All phases are given in rest frame.

In addition, we show the full wavelength coverage of the GB optical and NIR spectra of SN 2023ixf obtained between +72.16 and 761.97 days. These spectra are shown in Figures A1 and A2, respectively.

ORCID iDs

K. Medler https://orcid.org/0000-0001-7186-105X C. Ashall https://orcid.org/0000-0002-5221-7557 P. Hoeflich https://orcid.org/0000-0002-4338-6586 E. Baron https://orcid.org/0000-0001-5393-1608 J. M. DerKacy https://orcid.org/0000-0002-7566-6080 M. Shahbandeh https://orcid.org/0000-0002-9301-5302 T. Mera https://orcid.org/0000-0001-5888-2542 C. M. Pfeffer https://orcid.org/0000-0002-7305-8321 W. B. Hoogendam https://orcid.org/0000-0003-3953-9532 D. O. Jones https://orcid.org/0000-0002-6230-0151 S. Shiber https://orcid.org/0000-0001-6107-0887 E. Fereidouni https://orcid.org/0009-0001-9148-8421 O. D. Fox https://orcid.org/0000-0003-2238-1572 J. Jencson https://orcid.org/0000-0001-5754-4007 L. Galbany https://orcid.org/0000-0002-1296-6887 J. T. Hinkle https://orcid.org/0000-0001-9668-2920 M. A. Tucker https://orcid.org/0000-0002-2471-8442 B. J. Shappee https://orcid.org/0000-0003-4631-1149 M. E. Huber https://orcid.org/0000-0003-1059-9603 K. Auchettl https://orcid.org/0000-0002-4449-9152 C. R. Angus https://orcid.org/0000-0002-4269-7999 D. D. Desai https://orcid.org/0000-0002-2164-859X A. Do 6 https://orcid.org/0000-0003-3429-7845 A. V. Payne https://orcid.org/0000-0003-3490-3243 J. Shi https://orcid.org/0009-0008-3724-1824 M. Y. Kong https://orcid.org/0009-0005-5121-2884 S. Romagnoli https://orcid.org/0009-0003-8153-9576 A. Syncatto https://orcid.org/0009-0000-6821-9285 C. R. Burns https://orcid.org/0000-0003-4625-6629 G. Clayton https://orcid.org/0000-0002-0141-7436 M. Engesser https://orcid.org/0000-0003-0209-674X A. V. Filippenko https://orcid.org/0000-0003-3460-0103 S. Gomez https://orcid.org/0000-0001-6395-6702 E. Y. Hsiao https://orcid.org/0000-0003-1039-2928 T. de Jaeger https://orcid.org/0000-0001-6069-1139 J. Johansson https://orcid.org/0000-0001-5975-290X K. Krisciunas https://orcid.org/0000-0002-6650-694X S. Kumar https://orcid.org/0000-0001-8367-7591 J. Lu https://orcid.org/0000-0002-3900-1452 M. Matsuura https://orcid.org/0000-0002-5529-5593 P. A. Mazzali https://orcid.org/0000-0001-6876-8284

D. Milisavljevic https://orcid.org/0000-0002-0763-3885

^a Denotes observations taken in PRISM mode of IRTF/SpeX.

N. Morrell https://orcid.org/0000-0003-2535-3091 R. O'Steen https://orcid.org/0000-0002-2432-8946 S. Park https://orcid.org/0000-0001-7488-4337 M. M. Phillips https://orcid.org/0000-0003-2734-0796 A. P. Ravi https://orcid.org/0000-0002-7352-7845 A. Rest https://orcid.org/0000-0002-4410-5387 J. Rho https://orcid.org/0000-0003-3643-839X N. B. Suntzeff https://orcid.org/0000-0002-8102-181X A. Sarangi https://orcid.org/0000-0002-9820-679X N. Smith https://orcid.org/0000-0001-5510-2424 M. D. Stritzinger https://orcid.org/0000-0002-5571-1833 L. Strolger https://orcid.org/0000-0002-7756-4440 T. Szalai https://orcid.org/0000-0003-4610-1117 T. Temim https://orcid.org/0000-0001-7380-3144 S. Tinyanont https://orcid.org/0000-0002-1481-4676 S. D. Van Dyk https://orcid.org/0000-0001-9038-9950 L. Wang https://orcid.org/0000-0001-7092-9374 Q. Wang https://orcid.org/0000-0001-5233-6989 R. Wesson https://orcid.org/0000-0002-4000-4394 Y. Yang https://orcid.org/0000-0002-6535-8500 S. Zsíros https://orcid.org/0000-0001-7473-4208

References

```
Abac, A. G., Abbott, R., Abouelfettouh, I., et al. 2025, ApJ, 985, 183
Aldering, G., Adam, G., Antilogus, P., et al. 2002, Proc. SPIE, 4836, 61
Alvarez, P., Rodríguez, J. M., & Sánchez, F. 1998, NewAR, 42, 553
Anderson, J. P., Dessart, L., Gutierrez, C. P., et al. 2014, MNRAS, 441, 671
Andrews, J. E., Clayton, G. C., Wesson, R., et al. 2011a, AJ, 142, 45
Andrews, J. E., Sand, D. J., Valenti, S., et al. 2019, ApJ, 885, 43
Andrews, J. E., Sugerman, B. E. K., Clayton, G. C., et al. 2011b, ApJ, 731, 47
Arnett, W. D., Bahcall, J. N., Kirshner, R. P., & Woosley, S. E. 1989,
           . 27, 629
Ashall, C., Baron, E., DerKacy, J. M., et al. 2023a, Dust Our Luck? Measuring
   Molecule and Dust Formation in M101's Hydrogen-rich SN 2023ixf,
   JWST Proposal. Cycle 1, ID. #4522,
Ashall, C., Baron, E., DerKacy, J. M., et al. 2023b, Dust Our Luck? Measuring
   Molecule and Dust Formation in M101's Hydrogen-rich SN 2023ixf,
   JWST Proposal. Cycle 2, ID. #4575,
Ashall, C., Hoeflich, P., Baron, E., et al. 2024a, ApJ, 975, 203
Ashall, C., Hoeflich, P. A., Shahbandeh, M., et al. 2024b, Building the Legacy
   of Supernova 2023ixf: How Does Molecule Formation Lead to Dust?,
   JWST Proposal. Cycle 3, ID. #5290,
Astropy Collaboration, Price-Whelan, A. M., Lim, P. L., et al. 2022, ApJ,
   935, 167
Astropy Collaboration, Price-Whelan, A. M., Sipöcz, B. M., et al. 2018, AJ,
   156, 123
Astropy Collaboration, Robitaille, T. P., Tollerud, E. J., et al. 2013, A&A,
   558, A33
Baron, E., Ashall, C., DerKacy, J. M., et al. 2025, arXiv:2507.18753
Berger, E., Keating, G. K., Margutti, R., et al. 2023, ApJL, 951, L31
Bersten, M. C., Orellana, M., Folatelli, G., et al. 2024, A&A, 681, L18
Bevan, A. 2018, MNRAS, 480, 4659
Bevan, A., & Barlow, M. J. 2016, MNRAS, 456, 1269
Bevan, A., Wesson, R., Barlow, M. J., et al. 2019, MNRAS, 485, 5192
Biscaro, C., & Cherchneff, I. 2014, A&A, 564, A25
Bode, M. F., & Evans, A. 1980, MNRAS, 193, 21P
Böker, T., Beck, T. L., Birkmann, S. M., et al. 2023, PASP, 135, 038001
Bose, S., Dong, S., Elias-Rosa, N., et al. 2019, ApJL, 873, L3
Bostroem, K. A., Pearson, J., Shrestha, M., et al. 2023, ApJL, 956, L5
Burrow, A., Baron, E., Ashall, C., et al. 2020, ApJ, 901, 154
Bushouse, H., Eisenhamer, J., Dencheva, N., et al. 2022, JWST Calibration
  Pipeline, Tech. Rep., v1.7.0, Zenodo:10.5281/zenodo.7038885
Cardiel, N., Pascual, S., Gallego, J., et al. 2019, in ASP Conf. Ser. 523,
   Astronomical Data Analysis Software and Systems XXVII, ed.
   P. J. Teuben et al. (San Francisco, CA: ASP), 317
Catchpole, R., Glass, I., Karovska, M., et al. 1987, IAUC, 4457, 1
Chandra, P., Chevalier, R. A., Maeda, K., Ray, A. K., & Nayana, A. J. 2024,
   ApJL, 963, L4
Chevalier, R. A., & Fransson, C. 1987, Natur, 328, 44
Chiar, J. E., & Tielens, A. G. G. M. 2006, ApJ, 637, 774
```

```
Clayton, D. D., Deneault, E. A. N., & Meyer, B. S. 2001, ApJ, 562, 480
Clayton, G. C., Wesson, R., Fox, O. D., et al. 2025, ApJ, 991, 133
Cushing, M. C., Vacca, W. D., & Rayner, J. T. 2004, PASP, 116, 362
Davis, S., Hsiao, E. Y., Ashall, C., et al. 2019, ApJ, 887, 4
DerKacy, J., Ashall, C., Baron, E., et al. 2025, arXiv:2507.18785
Dessart, L., & Hillier, D. J. 2005, A&A, 437, 667
Dragulin, P., & Hoeflich, P. 2016, ApJ, 818, 26
Dubbeldam, M., Content, R., Allington-Smith, J. R., Pokrovski, S., &
  Robertson, D. J. 2000, Proc. SPIE, 4008, 1181
Dwek, E. 1983, ApJ, 274, 175
Dwek, E. 2006, Sci, 313, 178
Dwek, E., Galliano, F., & Jones, A. P. 2007, ApJ, 662, 927
Dwek, E., & Scalo, J. M. 1980, ApJ, 239, 193
Dyer, M. J., Ackley, K., Jiménez-Ibarra, F., et al. 2024, Proc. SPIE, 13094,
  130941X
Elmhamdi, A., Danziger, I. J., Chugai, N., et al. 2003, MNRAS, 338, 939
Ercolano, B., Barlow, M. J., & Sugerman, B. E. K. 2007, MNRAS, 375, 753
Fan, X., Strauss, M. A., Schneider, D. P., et al. 2003, AJ, 125, 1649
Fang, Q., Maeda, K., Kuncarayakti, H., et al. 2022, ApJ, 928, 151
Fang, Q., Maeda, K., Kuncarayakti, H., & Nagao, T. 2024, NatAs, 8, 111
Fedriani, R., Caratti o Garatti, A., Koutoulaki, M., et al. 2020, A&A,
  633, A128
Ferrari, L., Folatelli, G., Ertini, K., Kuncarayakti, H., & Andrews, J. E. 2024,
   A&A, 687, L20
Ferrarotti, A. S., & Gail, H. P. 2006, A&A, 447, 553
Flinner, N., Tucker, M. A., Beacom, J. F., & Shappee, B. J. 2023, RNAAS,
  7, 174
Folatelli, G., Ferrari, L., Ertini, K., Kuncarayakti, H., & Maeda, K. 2025,
       A, 698, A213
Fox, O., Szalai, T., Van Dyk, S. D., et al. 2024, JWST Proposal. Cycle 2,
  ID. #3921,
Gall, C., Hjorth, J., & Andersen, A. C. 2011, A&ARv, 19, 43
Gall, C., Hjorth, J., Watson, D., et al. 2014, Natur, 511, 326
Garzón, F., Balcells, M., Gallego, J., et al. 2022, A&A, 667, A107
Gerardy, C. L., Fesen, R. A., Höflich, P., & Wheeler, J. C. 2000, AJ, 119, 2968
Gordon, K. 2023, karllark/dust_extinction: OneRelationForAllWaves, v1.2,
  Zenodo:10.5281/zenodo.7799360
Gordon, K. D., Clayton, G. C., Decleir, M., et al. 2023, ApJ, 950, 86
Grefenstette, B. W., Brightman, M., Earnshaw, H. P., Harrison, F. A., &
  Margutti, R. 2023, ApJL, 952, L3
Groot, P. J., Bloemen, S., Vreeswijk, P. M., et al. 2022, Proc. SPIE, 12182,
  121821
Guetta, D., Langella, A., Gagliardini, S., & Della Valle, M. 2023, ApJL,
  955, L9
Hanuschik, R. W. 1988, PASA, 7, 446
Harris, C. R., Millman, K. J., van der Walt, S. J., et al. 2020, Natur, 585, 357
Hiramatsu, D., Tsuna, D., Berger, E., et al. 2023, ApJL, 955, L8
Hoeflich, P. 1988, PASA, 7, 434
Hoogendam, W. B., Ashall, C., Jones, D. O., et al. 2025a, ApJ, 988, 209
Hoogendam, W. B., Jones, D. O., Ashall, C., et al. 2025b, OJAp, 8, 120
Hosseinzadeh, G., Farah, J., Shrestha, M., et al. 2023, ApJL, 953, L16
Huber, M., Chambers, K. C., Flewelling, H., et al. 2015, ATel, 7153, 1
Hughes, D. H., Dunlop, J. S., & Rawlings, S. 1997, MNRAS, 289, 766
Hunter, J. D. 2007, CSE, 9, 90
Ilee, J. D., Oudmaijer, R. D., Wheelwright, H. E., & Pomohaci, R. 2018,
           , 477, 3360
Inserra, C., Turatto, M., Pastorello, A., et al. 2011, MNRAS, 417, 261
Itagaki, K. 2023, TNSTR, 2023-1158, 1, 2023
Iwata, Y., Akimoto, M., Matsuoka, T., et al. 2025, ApJ, 978, 138
Jacobson-Galán, W. V., Dessart, L., Margutti, R., et al. 2023, ApJL, 954, L42
Jakobsen, P., Ferruit, P., Alves de Oliveira, C., et al. 2022, A&A, 661, A80
Janka, H.-T. 2012, ARNPS, 62, 407
Janka, H.-T., Melson, T., & Summa, A. 2016, ARNPS, 66, 341
Jencson, J. E., Pearson, J., Beasor, E. R., et al. 2023, ApJL, 952, L30
Jerkstrand, A., Fransson, C., Maguire, K., et al. 2012, A&A, 546, A28
Kendrew, S., Scheithauer, S., Bouchet, P., et al. 2015, PASP, 127, 623
Khokhlov, A., & Höflich, P. 2001, in AIP Conf. Ser. 556, Explosive
  Phenomena in Astrophysical Compact Objects, ed. H.-Y. Chang et al.
  (Melville, NY: AIP), 301, doi:10.1063/1.1368287
Kilpatrick, C. D., Foley, R. J., Jacobson-Galán, W. V., et al. 2023, ApJL,
  952, L23
Kotak, R., Meikle, P., Pozzo, M., et al. 2006, ApJL, 651, L117
Kotak, R., Meikle, P., van Dyk, S. D., Höflich, P. A., & Mattila, S. 2005,
   ApJL, 628, L123
Kotak, R., Meikle, W. P. S., Farrah, D., et al. 2009, ApJ, 704, 306
Kumar, A., Dastidar, R., Maund, J. R., Singleton, A. J., & Sun, N.-C. 2025,
```

MNRAS, 538, 659

```
Kuncarayakti, H., Folatelli, G., Maeda, K., et al. 2020, ApJ, 902, 139
Lantz, B., Aldering, G., Antilogus, P., et al. 2004, Proc. SPIE, 5249, 146
Law, D., Diaz, R., Sosey, M., et al. 2025, JWST Pipeline Notebooks, Tech.
   Rep, v1.1.0, Zenodo:10.5281/zenodo.15571377
Leonard, D. C., Filippenko, A. V., Gates, E. L., et al. 2002, PASP, 114, 35
Li, G., Wang, X., Yang, Y., et al. 2025, arXiv:2504.03856
Li, H., & McCray, R. 1992, ApJ, 387, 309
Liljegren, S., Jerkstrand, A., & Grumer, J. 2020, A&A, 642, A135
Liu, C., Chen, X., Er, X., et al. 2023, ApJL, 958, L37
Liu, W., & Dalgarno, A. 1994, ApJ, 428, 769
Liu, W., & Dalgarno, A. 1995, ApJ, 454, 472
Liu, W., Dalgarno, A., & Lepp, S. 1992, ApJ, 396, 679
Lucy, L. B., Danziger, I. J., Gouiffes, C., & Bouchet, P. 1989, in IAU
   Colloquium 120: Structure and Dynamics of the Interstellar Medium, ed.
   G. Tenorio-Tagle, M. Moles, & J. Melnick, 350 (Berlin: Springer), 164
Maeda, K., Kawabata, K., Mazzali, P. A., et al. 2008, Sci, 319, 1220
Maguire, K., Di Carlo, E., Smartt, S. J., et al. 2010, MNRAS, 404, 981
Maiolino, R., Schneider, R., Oliva, E., et al. 2004, Natur, 431, 533
Margutti, R., Soderberg, A. M., Chomiuk, L., et al. 2012, ApJ, 751, 134
Martí-Devesa, G., Cheung, C. C., Di Lalla, N., et al. 2024, A&A, 686, A254
Matheson, T., Filippenko, A. V., Barth, A. J., et al. 2000, AJ, 120, 1487
Maund, J. R. 2017, MNRAS, 469, 2202
McCarthy, J. K., Cohen, J. G., Butcher, B., et al. 1998, Proc. SPIE, 3355, 81
Medler, K., Ashall, C., Shahbandeh, M., et al. 2025, arXiv:2505.18507
Meikle, W. P. S., Kotak, R., Farrah, D., et al. 2011, ApJ, 732, 109
Meikle, W. P. S., Mattila, S., Pastorello, A., et al. 2007, ApJ, 665, 608
Mera, T., Ashall, C., Hoeflich, P., et al. 2025, arXiv:2510.09600
Michel, P. D., Mazzali, P. A., Perley, D. A., Hinds, K. R., & Wise, J. L. 2025,
   MNRAS, 539, 633
Milisavljevic, D., Fesen, R. A., Gerardy, C. L., Kirshner, R. P., & Challis, P.
   2010, ApJ, 709, 1343
Modjaz, M., Kirshner, R. P., Blondin, S., Challis, P., & Matheson, T. 2008,
    pJL, 687, L9
Müller, B., Heger, A., Liptai, D., & Cameron, J. B. 2016, MNRAS, 460, 742
Müller Bravo, T. E. 2023, temuller/idsred: First Release!, v0.1.0, Zenodo:10.
   5281/zenodo.7851772
Nayana, A. J., Margutti, R., Wiston, E., et al. 2025, ApJ, 985, 51
Neustadt, J. M. M., Kochanek, C. S., & Smith, M. R. 2024, MNRAS,
   527, 5366
Niculescu-Duvaz, M., Barlow, M. J., Bevan, A., et al. 2022, MNRAS,
   515, 4302
Niu, Z., Sun, N.-C., Maund, J. R., et al. 2023, ApJL, 955, L15
Oke, J. B., Cohen, J. G., Carr, M., et al. 1995, PASP, 107, 375
Panjkov, S., Auchettl, K., Shappee, B. J., et al. 2024, PASA, 41, e059
Park, S. H., Rho, J., Yoon, S.-C., et al. 2025, arXiv:2507.11877
Pascual, S., Cardiel, N., Garzón, F., et al. 2019, in ASP Conf. Ser. 521,
   Astronomical Data Analysis Software and Systems XXVI, ed.
   M. Molinaro, K. Shortridge, & F. Pasian (San Francisco, CA: ASP), 232
Pascual, S., Gallego, J., Cardiel, N., & Eliche-Moral, M. C. 2010, in ASP
   Conf. Ser. 434. Astronomical Data Analysis Software and Systems XIX.
   ed. Y. Mizumoto, K. I. Morita, & M. Ohishi (San Francisco, CA: ASP), 353
Perley, D., & Gal-Yam, A. 2023, TNSTR, 2023-119, 1
Perrin, M. D., Sivaramakrishnan, A., Lajoie, C.-P., et al. 2014, Proc. SPIE,
   9143, 91433X
Pledger, J. L., & Shara, M. M. 2023, ApJL, 953, L14
Podsiadlowski, P. 1992, PASP, 104, 717
Pozzo, M., Meikle, W. P. S., Fassia, A., et al. 2004, MNRAS, 352, 457
Pozzo, M., Meikle, W. P. S., Rayner, J. T., et al. 2007, MNRAS, 375, 416
Qin, Y.-J., Zhang, K., Bloom, J., et al. 2024, MNRAS, 534, 271
Ransome, C. L., Villar, V. A., Tartaglia, A., et al. 2024, ApJ, 965, 93
Ravensburg, E., Carenza, P., Eckner, C., & Goobar, A. 2024, PhRvD, 109,
Ravi, A. P., Rho, J., Park, S., et al. 2023, ApJ, 950, 14
Rayner, J. T., Toomey, D. W., Onaka, P. M., et al. 2003, PASP, 115, 362
Rho, J., Evans, A., Geballe, T. R., et al. 2021, ApJ, 908, 232
Rho, J., Park, S. H., Arendt, R., et al. 2024, ApJL, 969, L9
Riess, A. G., Yuan, W., Macri, L. M., et al. 2022, ApJL, 934, L7
Roche, P. F., Aitken, D. K., & Smith, C. H. 1991, MNRAS, 252, 39P
Roche, P. F., Aitken, D. K., Smith, C. H., & James, S. D. 1989, Natur,
  337, 533
Rockosi, C., Stover, R., Kibrick, R., et al. 2010, Proc. SPIE, 7735, 77350R
```

```
Sahu, D. K., Anupama, G. C., Srividya, S., & Muneer, S. 2006, MNRAS,
  372, 1315
Sarangi, A. 2022, A&A, 668, A57
Sarangi, A., & Cherchneff, I. 2015, A&A, 575, A95
Sarangi, A., Dwek, E., & Arendt, R. G. 2018, ApJ, 859, 66
Sarmah, P. 2024, JCAP, 2024, 083
Scheck, L., Kifonidis, K., Janka, H. T., & Müller, E. 2006, A&A, 457, 963
Schlafly, E. F., & Finkbeiner, D. P. 2011, ApJ, 737, 103
Schneider, R., Ferrara, A., & Salvaterra, R. 2004, MNRAS, 351, 1379
Shahbandeh, M., Ashall, C., Hoeflich, P., et al. 2024, arXiv:2401.14474
Shahbandeh, M., Fox, O. D., Temim, T., et al. 2025, ApJ, 985, 262
Shahbandeh, M., Hsiao, E. Y., Ashall, C., et al. 2022, ApJ, 925, 175
Shahbandeh, M., Sarangi, A., Temim, T., et al. 2023, MNRAS, 523, 6048
Shappee, B. J., Prieto, J. L., Grupe, D., et al. 2014, ApJ, 788, 48
Sharp, C. M., & Hoeflich, P. 1990, Ap&SS, 171, 213
Singh, A., Teja, R. S., Moriya, T. J., et al. 2024, ApJ, 975, 132
Singh, P. D. 1975, A&A, 44, 411
Sluder, A., Milosavljević, M., & Montgomery, M. H. 2018, MNRAS, 480, 5580
Smartt, S. J., Eldridge, J. J., Crockett, R. M., & Maund, J. R. 2009, MNRAS,
  395, 1409
Smith, N., Foley, R. J., & Filippenko, A. V. 2008, ApJ, 680, 568
Smith, N., Pearson, J., Sand, D. J., et al. 2023, ApJ, 956, 46
Smith, N., Silverman, J. M., Filippenko, A. V., et al. 2012, AJ, 143, 17
Snow, C. P., & Rideal, E. K. 1929, RSPSA, 125, 462
Soraisam, M. D., Szalai, T., Van Dyk, S. D., et al. 2023, ApJ, 957, 64
Spyromilio, J., & Leibundgut, B. 1996, MNRAS, 283, L89
Spyromilio, J., Meikle, W. P. S., Learner, R. C. M., & Allen, D. A. 1988,
  Natur, 334, 327
Stritzinger, M., Taddia, F., Fransson, C., et al. 2012, ApJ, 756, 173
Stritzinger, M., Valerin, G., Elias-Rosa, N., et al. 2023, TNSAN, 145, 1
Szalai, T., & Van Dyk, S. V. 2023, ATel, 16042, 1
Szalai, T., & Vinkó, J. 2013, A&A, 549, A79
Szalai, T., Vinkó, J., Balog, Z., et al. 2011, A&A, 527, A61
Szalai, T., Vinkó, J., Könyves-Tóth, R., et al. 2019, ApJ, 876, 19
Taubenberger, S., Valenti, S., Benetti, S., et al. 2009, MNRAS, 397, 677
Teja, R. S., Singh, A., Basu, J., et al. 2023, ApJL, 954, L12
Thwaites, J., Vandenbroucke, J., Santander, M. & IceCube Collaboration
  2023, ATel, 16043, 1
Tinyanont, S., Fox, O. D., Shahbandeh, M., et al. 2025, ApJ, 985, 198
Tinyanont, S., Lau, R. M., Kasliwal, M. M., et al. 2019, ApJ, 887, 75
Tonry, J. L., Denneau, L., Heinze, A. N., et al. 2018, PASP, 130, 064505
Tucker, M. A., Hinkle, J., Angus, C. R., et al. 2024, ApJ, 976, 178
Tucker, M. A., Shappee, B. J., Huber, M. E., et al. 2022, PASP, 134, 124502
Utrobin, V. P., & Chugai, N. N. 2009, A&A, 506, 829
Utrobin, V. P., & Chugai, N. N. 2017, MNRAS, 472, 5004
Valiante, R., Schneider, R., Bianchi, S., & Andersen, A. C. 2009, MNRAS,
  397, 1661
van Breemen, J. M., Min, M., Chiar, J. E., et al. 2011, A&A, 526, A152
Van Dyk, S. D., Srinivasan, S., Andrews, J. E., et al. 2024a, ApJ, 968, 27
Van Dyk, S. D., Szalai, T., Cutri, R. M., et al. 2024b, ApJ, 977, 98
Vasylyev, S. S., Yang, Y., Filippenko, A. V., et al. 2023, ApJL, 955, L37
Virtanen, P., Gommers, R., Oliphant, T. E., et al. 2020, NatMe, 17, 261
Wang, T., & Burrows, A. 2024, ApJ, 962, 71
Watson, D., Christensen, L., Knudsen, K. K., et al. 2015, Natur, 519, 327
Wesson, R., Barlow, M. J., Matsuura, M., & Ercolano, B. 2015, MNRAS,
  446, 2089
Williams, B. F., Peterson, S., Murphy, J., et al. 2014, ApJ, 791, 105
Wilson, J. C., Henderson, C. P., Herter, T. L., et al. 2004, Proc. SPIE,
   5492, 1295
Wooden, D. H., Rank, D. M., Bregman, J. D., et al. 1993, ApJSApJS, 88, 477
Woosley, S. E., Heger, A., & Weaver, T. A. 2002, RvMP, 74, 1015
Woosley, S. E., Pinto, P. A., & Ensman, L. 1988, ApJ, 324, 466
Woosley, S. E., & Weaver, T. A. 1995, ApJS, 101, 181
Xiang, D., Mo, J., Wang, L., et al. 2024, SCPMA, 67, 219514
Yamanaka, M., Fujii, M., & Nagayama, T. 2023, PASJ, 75, L27
Yang, Y.-P., Liu, X., Pan, Y., et al. 2024, ApJ, 969, 126
Yaron, O., & Gal-Yam, A. 2012, PASP, 124, 668
Zhang, J., Lin, H., Wang, X., et al. 2023, SciBu, 68, 2548
Zheng, W., Dessart, L., Filippenko, A. V., et al. 2025, ApJ, 988, 61
Zimmerman, E. A., Irani, I., Chen, P., et al. 2024, Natur, 627, 759
Zsíros, S., Szalai, T., De Looze, I., et al. 2024, MNRAS, 529, 155
```